JGR Oceans

RESEARCH ARTICLE
10.1029/2023JC020593

Reduction of Drag Coefficient Due To Misaligned Wind-Waves

Emma Manzella[1], Tetsu Hara[1], and Peter P. Sullivan[2]

[1]Graduate School of Oceanography, University of Rhode Island, Narragansett, RI, USA, [2]National Center for Atmospheric Research, Boulder, CO, USA

Key Points:

- Large eddy simulations are preformed to study wind over misaligned surface waves
- Drag coefficient is reduced due to misaligned surface waves for all wave ages under wind-driven wave conditions
- Drag reduction can occur even when wave form drag is positive

Correspondence to:

T. Hara,
tetsuhara@uri.edu

Citation:

Manzella, E., Hara, T., & Sullivan, P. P. (2024). Reduction of drag coefficient due to misaligned wind-waves. *Journal of Geophysical Research: Oceans*, *129*, e2023JC020593. https://doi.org/10.1029/2023JC020593

Received 19 OCT 2023
Accepted 6 APR 2024

Author Contributions:

Conceptualization: Emma Manzella, Tetsu Hara
Data curation: Emma Manzella, Tetsu Hara
Formal analysis: Emma Manzella, Tetsu Hara
Funding acquisition: Tetsu Hara
Investigation: Emma Manzella, Tetsu Hara
Methodology: Emma Manzella, Tetsu Hara, Peter P. Sullivan
Project administration: Tetsu Hara
Resources: Emma Manzella, Tetsu Hara
Software: Emma Manzella, Tetsu Hara, Peter P. Sullivan
Supervision: Tetsu Hara
Validation: Emma Manzella, Tetsu Hara
Visualization: Emma Manzella, Tetsu Hara
Writing – original draft: Emma Manzella, Tetsu Hara, Peter P. Sullivan
Writing – review & editing: Emma Manzella, Tetsu Hara, Peter P. Sullivan

Abstract Recent field observations suggest that the air-sea momentum flux (or the drag coefficient) is significantly reduced when the dominant wind-forced surface waves are misaligned from local wind. Such conditions may occur under rapidly changing strong winds (such as under tropical cyclones) or in coastal shallow waters where waves are refracted by bottom topography. A recent Large Eddy Simulation (LES) study also shows that the drag coefficient is reduced by a misaligned strongly forced wave train (with a small wave age of 1.37). In order to investigate more realistic field conditions, this study employs LES to examine the effect of a misaligned (up to 90°) surface wave train over a wide range of wave age up to 10.95. For all wave ages examined, the drag coefficient is reduced compared to the flat surface condition when the misalignment angle exceeds around 22.5°–45°. The drag reduction may occur even if the form drag of the wave train is positive.

Plain Language Summary This study uses computer simulations to investigate turbulent wind blowing over ocean surface waves that are misaligned (propagate in different directions) from the wind. The study focuses on frictional wind forcing (wind stress) imparted on the ocean surface, because the wind stress is an important boundary condition for ocean, atmospheric, and surface wave models. Surface waves can be misaligned from wind when the wind field rapidly changes such as during tropical storms or in shallow water where wave directions are modified by varying water depth. When waves propagate slower than wind in the wind direction, the waves increase the wind stress compared to flat surface (no wave) conditions. However, this study finds that the wind stress is reduced, that is, the ocean surface becomes smoother, when the misalignment angle between wind and waves exceeds about 22.5°–45°.

1. Introduction

Atmosphere, ocean, as well as coupled ocean-atmosphere models require accurate parameterizations of air-sea fluxes of energy, momentum, heat, and gases. In particular, the momentum flux is the main forcing of the upper ocean and the key bottom boundary (friction) condition for the atmosphere. The drag coefficient C_d relates the neutral (stability-corrected) 10 m wind speed to the surface stress (or friction velocity u_*). When wind and waves are in equilibrium, that is, when the surface wave field is fully developed, the drag coefficient can be parameterized as a function of the neutral 10 m wind speed alone. However, the ocean surface wave fields are frequently in non-equilibrium conditions, that is, waves are growing/decaying and/or are misaligned from the local wind field. It is well documented that a better understanding of sea-state dependent drag coefficient is needed.

The wave age is often used to describe the development of a wind-wave field through the ratio between peak wave phase speed c_p to the surface friction velocity u_*. The wind-driven wave regime is generally thought to be around $c_p/u_* < 15$, when the dominant waves propagate slower than the wind and are pushed by the wind. Wave-driven wind conditions (or swell) occur roughly at $c_p/u_* > 20$, meaning that the dominant waves are developed enough to travel faster than the local wind field above, and can actually "drive" the wind. Many studies have been conducted to investigate the effect of wave age and wave slope on air-sea fluxes (Banner, 1990; Belcher et al., 1993; Donelan, 2004; Donelan et al., 1993, 2006; Edson et al., 2013; Husain et al., 2019; Makin & Kudryavtsev, 1999).

Large Eddy Simulation (LES) is a powerful tool to investigate the wind field over surface waves and the resulting drag coefficient. Recently, Husain et al. (2019) used LES coupled with laboratory PIV (particle image velocimetry) observations to examine strongly forced conditions (low wave age) over steep waves, and were able to observe intermittent air-flow separation events and their impacts on the wind stress and the drag coefficient. More recent studies investigated the effect of opposing wind over waves (Cao et al., 2020; Husain et al., 2022b). Both studies found that opposing waves increased wave decay as wave age increased, while the latter study also found

that the equivalent roughness length (or the drag coefficient) for wind opposing waves was enhanced as the wave age increased, in contrast to reduction of the roughness length for wind following waves as the wave age increased.

Misalignment between wind and waves (i.e., the difference between the wave direction and the wind speed direction) can occur in both the wind-driven wave conditions and the wave-driven wind conditions. Under the wave-driven wind conditions, misalignment occurs when swell from distant storms is misaligned with the local wind field (Hanley et al., 2010). Patton et al. (2019) found that the equivalent roughness length increased with misalignment under swell-dominated conditions.

Under wind-driven wave conditions, misalignment can occur due to rapidly changing strong wind or due to wave refraction in shallow coastal water. Potter et al. (2022) found a reduction in the drag coefficient as misalignment increases in an observational study of near-shore air-sea momentum flux. Misalignment is particularly common under tropical cyclones given their rapidly varying wind structure. Zhou et al. (2022) found that this misalignment occurs primarily on the left to far front-right side of the storm (in the northern hemisphere), and found significant evidence for drag reduction as misalignment increased, which was also reported by Sheng et al. (2022). These observations clearly suggest that there is need for a better understanding of how wind-wave misalignment affects air-sea fluxes and drag coefficient under wind-driven wave conditions.

It is well documented that the drag coefficient increases with wind speed at low to moderate wind speeds, but it becomes constant or even decreases under very high (tropical cyclone) wind speeds (Holthuijsen et al., 2012; Hsu et al., 2019; Powell et al., 2003). The physical mechanism of the drag reduction in high winds is not fully understood. However, the recent observations under tropical cyclones (Sheng et al., 2022; Zhou et al., 2022) show that the drag coefficient further decreases as the wind-wave misalignment increases, suggesting that dominant waves play a significant role in modifying the drag coefficient under tropical cyclones.

In Husain et al. (2022a), initial steps were taken to investigate misalignment effects under a low wave age (1.37), and the results indicated that a reduction in drag occurred for wind over waves at an angle of $\theta = 67.5°$. However, this wave age is significantly lower than those in the observed field conditions. This study aims to extend the work of Husain et al. (2022a) and investigate misalignment (0–90°) effects for a wide range of wave age, from strongly forced to weakly forced conditions (wave age up to 10.95) in order to obtain a more comprehensive understanding of the effects of misalignment on drag reduction, as well as impacts on the wave form drag and the wave growth/decay rate. We are particularly interested in the results of the high wave age case, as it is in the range of wave age that can occur during tropical cyclones. This study also aims to better understand the physical mechanisms that cause the drag reduction.

2. Methods

2.1. Large Eddy Simulation Set Up

Large Eddy Simulations (LES) are conducted in order to examine the effects of misaligned surface waves on the drag coefficient. The simulations employ the same methodology as those of the previous studies (Hara & Sullivan, 2015; Husain et al., 2019, 2022a, 2022b; Sullivan et al., 2014), which simulate a pressure driven channel flow over a prescribed periodic wave surface. Since we are focused on studying the air-flow, the wave motion is prescribed and decoupled from the air. The physical coordinates are as follows: time t, along-wave x, cross-wave y, and vertical coordinate z pointing upwards and $z = 0$ is at the mean water surface. The computational domain is 3D rectangular with doubly periodic horizontal boundaries and a free slip flat top boundary condition. We transform the vertical physical coordinate z to a wave following computational vertical coordinate ζ^{LES}:

$$z = \zeta^{LES} + h(x, t)\left(1 - \frac{\zeta^{LES}}{l_\zeta}\right)^3 \tag{1}$$

so that the wavy surface $z = h\,(x, t)$ is mapped to a flat surface $\zeta^{LES} = 0$, where l_ζ is the height of the vertical computational domain (Figure 1 in Sullivan et al., 2014).

Following Husain et al. (2022a, 2022b), the wave train is prescribed as $h\,(x, t) = a\cos(kx - \omega t)$, where a is the wave amplitude, k is the wavenumber, ω is the angular frequency, and $c = \omega/k = \sqrt{g/k}$ is the phase speed. The

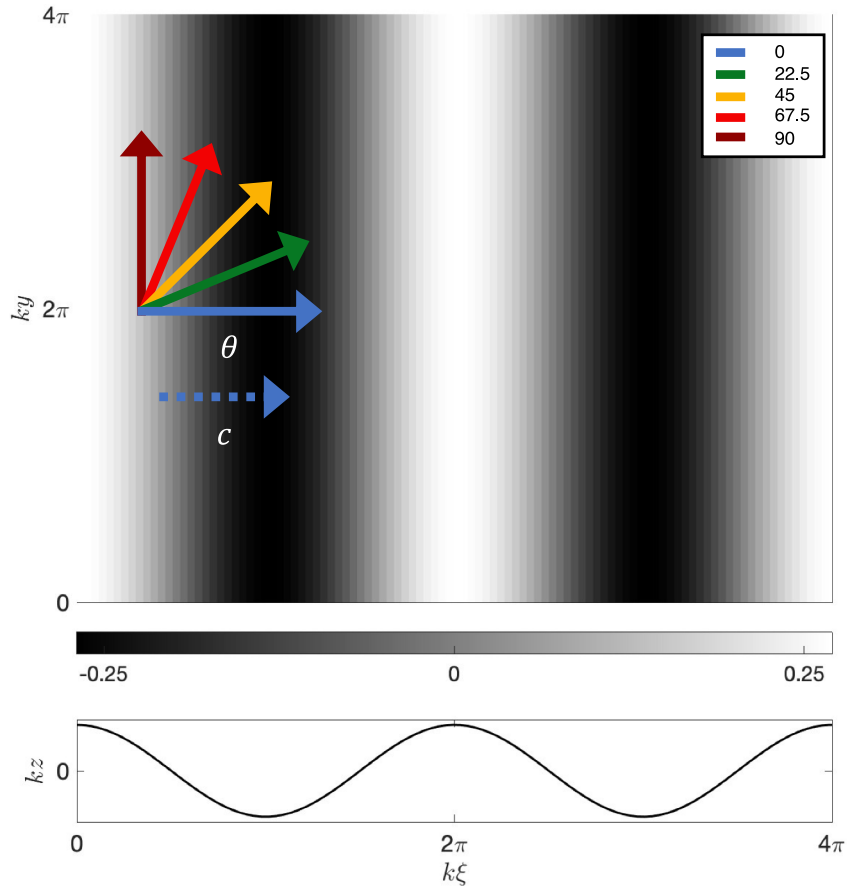

Figure 1. Wind stress direction θ and wave phase speed c shown over wave shape. Wind stress direction θ varies from $\theta = 0$–90° and is aligned with $-\Delta p$. The direction of wave phase speed c remains constant for all cases.

linear wave orbital velocities, $u = a\omega \cos(kx - \omega t)$ and $w = a\omega \sin(kx - \omega t)$, are used as the surface boundary condition for the LES. We choose the linear wave field since Husain et al. (2022b) found relatively minor differences in the wind field if the second-order nonlinear Stokes wave solution is used at the bottom boundary. Since the simulations are performed over a single wave train, the wave age is defined as c/u_* from here on.

The simulations are preformed for three wave ages ($c/u_* = 1.37, 5.48, 10.95$). Following Husain et al. (2022a), for the lowest wave age ($c/u_* = 1.37$) the domain size is $l_x \times l_y \times l_\zeta = 5\lambda \times 5\lambda \times \lambda$, where $\lambda = 2\pi/k$ is the wave length, and the domain is discretized with $(N_x, N_y, N_\zeta) = (256, 256, 128)$ grid points. The horizontal resolution is constant at 0.01953λ, but the vertical spacing is not fixed in order to allow for a finer resolution near the surface. The first point off the wavy surface is at $\zeta^{LES} = 0.0065\lambda$ and the ratio between neighboring cells is held constant at 1.0028. For the middle and highest wave ages ($c/u_* = 5.48, 10.95$) the LES domain height l_ζ is increased to 2.435λ and N_ζ is doubled to 256, since the wave-induced perturbations reach higher as the wave age increases (Husain et al., 2022b).

2.2. Wind Forcing

The simulations are performed with the fixed wave propagation direction (x) and applying wind in a varying direction forced by a horizontal pressure gradient $\nabla p = \left(\frac{\partial p}{\partial x}, \frac{\partial p}{\partial y}\right)$. This pressure gradient is balanced by the surface wind stress $\tau_s = u_*^2 = |\nabla p| l_\zeta$ and the wind stress direction θ is in the same direction as $-\nabla p$ (Figure 1). The wind stress decreases linearly until it reaches 0 at the top. The linearly decreasing stress, which is inherent in a pressure-driven channel flow, has been found not to significantly affect the turbulence in the wave boundary layer provided the channel height is sufficiently large (Husain et al., 2019).

2.3. Sub-Grid Scale Parameterizations

While the dominant scale turbulence is explicitly resolved, sub-grid scale (SGS) energy and fluxes are modeled using the SGS parameterizations that follow the conventional turbulent kinetic energy (TKE) closure described by Moeng (1984), Moeng and Sullivan (2015), and Sullivan et al. (2014). Along the bottom boundary the local instantaneous tangential stress is parameterized based on the local instantaneous wind shear by applying the law of the wall following Hara and Sullivan (2015) and Husain et al. (2019, 2022b, 2022a). We prescribe a constant background roughness z_{ob} to account for the form drag of SGS waves and surface viscous stress.

2.4. Simulations

The simulations are performed for five wind stress directions ($\theta = 0, 22.5, 45, 67.5, 90°$) and three wave ages ($c/u_* = 1.37, 5.48, 10.95$) for a total of 15 cases. For $c/u_* = 5.48, 10.95$, each simulation is run for about 200,000 time steps and then averaged over the last 60,000 time steps after convergence has been satisfied, while for $c/u_* = 1.37$ simulations are run for about 100,000 time steps since less iterations are needed for convergence for the smaller domain size. These wave ages are identical to the lowest, middle, and highest values in Husain et al. (2022b), who only investigated wind following and opposing waves ($\theta = 0, 180°$). Husain et al. (2022a) investigated three misaligned conditions ($\theta = 22.5, 45, 67.5°$) for the lowest wave age only ($c/u_* = 1.37$). In this study we expand upon these previous studies to cover all five directions and all three wave ages. In particular, the highest wave age ($c/u_* = 10.95$) corresponds to typical conditions of misaligned dominant waves seen under tropical cyclone wind forcing as reported by Zhou et al. (2022).

Since detailed sensitivity studies of varying wave slope, background roughness, and surface drift current velocity have been conducted by Husain et al. (2019), in this study we set a constant wave slope $ak = 0.27$ and a constant background roughness $kz_{ob} = 2.7 \times 10^{-3}$ and assume no surface drift current following Husain et al. (2022a, 2022b).

2.5. Data Analysis

The LES results calculated in the ζ^{LES} coordinate are first mapped in the physical z coordinate. We then introduce a horizontal coordinate $\xi = x - ct$ that moves with the wave phase speed, so that the wave shape is frozen and the wave phase averaged variables become steady in the (ξ, y, z) coordinates. Next, the vertical coordinate z is mapped again to the wave-following coordinate ζ defined as

$$z = \zeta + a\cos(k\xi)e^{-k\zeta} \tag{2}$$

with the Jacobian coordinate transformation $J = \frac{\partial \zeta}{\partial z}$ as outlined in Hara and Sullivan (2015). This wave-following coordinate ζ is preferable to ζ^{LES} since it is independent of the LES domain height and exponentially approaches the z coordinate away from the surface. Constant ζ surfaces are defined such that they resemble the wave shape near the wave and become flat far away from the surface. This coordinate allows us to investigate the turbulent wind field very close to the wavy surface.

In the (ξ, y, ζ) coordinates, we next apply the triple decomposition of variables such that horizontal mean ($\langle\psi\rangle$), wave coherent ($\tilde{\psi}$), and turbulent (ψ') components of each variable ψ can be examined:

$$\psi = \overline{\psi} + \psi' = \langle\psi\rangle + \tilde{\psi} + \psi' \tag{3}$$

where $\overline{\psi}$ is the phase average. Applying this triple decomposition to the momentum equations also allows us to derive the horizontally averaged momentum equation

$$\frac{\langle\tau_{13}^{w}\rangle}{u_*^2} + \frac{\langle\tau_{13}^{p}\rangle}{u_*^2} + \frac{\langle\tau_{13}^{t}\rangle}{u_*^2} + \frac{\frac{\partial p}{\partial \xi}\zeta}{u_*^2} = \cos\theta \tag{4}$$

$$\frac{\langle\tau_{23}^{w}\rangle}{u_*^2} + \frac{\langle\tau_{23}^{t}\rangle}{u_*^2} + \frac{\frac{\partial p}{\partial y}\zeta}{u_*^2} = \sin\theta \tag{5}$$

where $(\langle\tau_{13}^w\rangle, \langle\tau_{23}^w\rangle) = (\langle\tilde{u}\tilde{W}\rangle, \langle\tilde{v}\tilde{W}\rangle)$ is the wave-coherent stress, and $(\langle\tau_{13}^p\rangle, 0) = \left(\langle\frac{1}{J}\overline{p}\frac{\partial\zeta}{\partial\xi}\rangle, 0\right)$ is the pressure (form) stress. The wave-induced stress comprises these two terms. The turbulent stress $(\langle\tau_{13}^t\rangle, \langle\tau_{23}^t\rangle) = \left(\langle u'W'\rangle, \langle v'W'\rangle\right)$ is further composed of the resolved turbulent stress and the SGS parameterization. Notice that the contravariant vertical velocity W is used to define the fluxes such that it is always perpendicular to constant ζ surfaces:

$$W = \frac{1}{J}u\frac{\partial\zeta}{\partial\xi} + w \tag{6}$$

For more details, as well as for the derivation of the energy equations, refer to Hara and Sullivan (2015).

3. Results

3.1. Horizontally Averaged Wind Profiles and Equivalent Roughness Length

Since the main objective of this study is to investigate reduction of the equivalent roughness length (or the drag coefficient) due to misaligned surface waves, we first present the vertical profiles of horizontally averaged wind speed and wind shear for all cases (five angles and three wave ages) in Figure 2. In this figure misalignment increases from $\theta = 0°$ to $\theta = 90°$ as color warms from blue to dark red. All profiles are displayed up to $k\zeta = 4$ because the LES results above are influenced by the flat top boundary (at $k\zeta \approx kz = 6.28$ or 15.3). The solid colored lines in Figure 2 show vertical profiles of wind magnitude (top row), wind direction (second row), wind shear magnitude (third row), and wind shear direction (bottom row). On each plot, the solid black line represents the flat wall (no wave) profile with the background roughness of $kz_{ob} = 2.7 \times 10^{-3}$ corresponding to the linearly decreasing stress profile. For reference, the dashed black line shows the flat wall profile corresponding to the constant stress profile. The dashed black line is not visible when it is identical to the black solid line. In the bottom row, the colored dashed lines show the turbulent stress direction, which will be discussed later.

3.1.1. Wind Speed Magnitude Profile

First let us examine the mean wind speed magnitude. In all cases, the wind magnitude profiles become roughly parallel to the flat wall profile (solid black line) above around $k\zeta = 1$). (We call the region above $k\zeta = 1$ "far-field" from here on). Since the wind stress is fixed, if the far-field wind speed is larger (smaller) than the flat wall case, the equivalent roughness length (and the drag coefficient) has decreased (increased) relative to the flat wall condition because of the imposed wave train. The far-field wind speed magnitude is reduced compared to the flat wall profile at all wave ages if wind and waves are aligned, as discussed in Husain et al. (2022b). As misalignment increases, the far-field wind increases at all wave ages. For $c/u_* = 1.37$ and 5.48 the far-field wind at $\theta = 45°$ becomes similar to the flat wall case and becomes larger (drag reduction) at $\theta = 67.5°$ and 90°. The drag reduction occurs at even smaller θ at the high wave age of 10.95.

3.1.2. Equivalent Roughness Length

We summarize the values of z_o/z_{ob}, that is, the ratio of the equivalent roughness length with the wave train (z_0) to the background roughness length (z_{ob}), in Figure 3 and Tables 1 and 2. If this value is larger (smaller) than 1, the roughness length and the drag coefficient have increased (decreased) due to the imposed wave train. In Figure 3 black lines represent $c/u_* = 1.37$, red lines $c/u_* = 5.48$, and blue lines $c/u_* = 10.95$. The equivalent roughness length z_o has been calculated by horizontally shifting the flat wall wind profile (black solid line in the top panels of Figure 2) until it matches the far-field wind speed magnitude with the wave train (colored lines), and then finding where the shifted flat wall profile reaches 0. Since the far-field wind profiles with waves are not perfectly parallel to the flat wall profile, they are matched at two different heights in order to account for the uncertainty of the calculations. For $c/u_* = 5.48$ and 10.95 matching is done at $k\zeta = 3$ (solid lines in Figure 3) and $k\zeta = 6$ (dashed lines). Recall that a smaller domain size is used for the lowest wave age, so matching for $c/u_* = 1.37$ is done at the smaller $k\zeta$ values of 2–4.

When wind and waves are aligned, there is an enhancement in the roughness. The enhancement is the most significant for $c/u_* = 1.37$ and decreases as the wave age increases, as seen in Husain et al. (2022b). As misalignment increases, the roughness decreases such that reduction in the drag compared to the flat wall case is seen (i.e., the waves are making the surface smoother) roughly at $\theta > 45°$ for low and middle wave ages and at

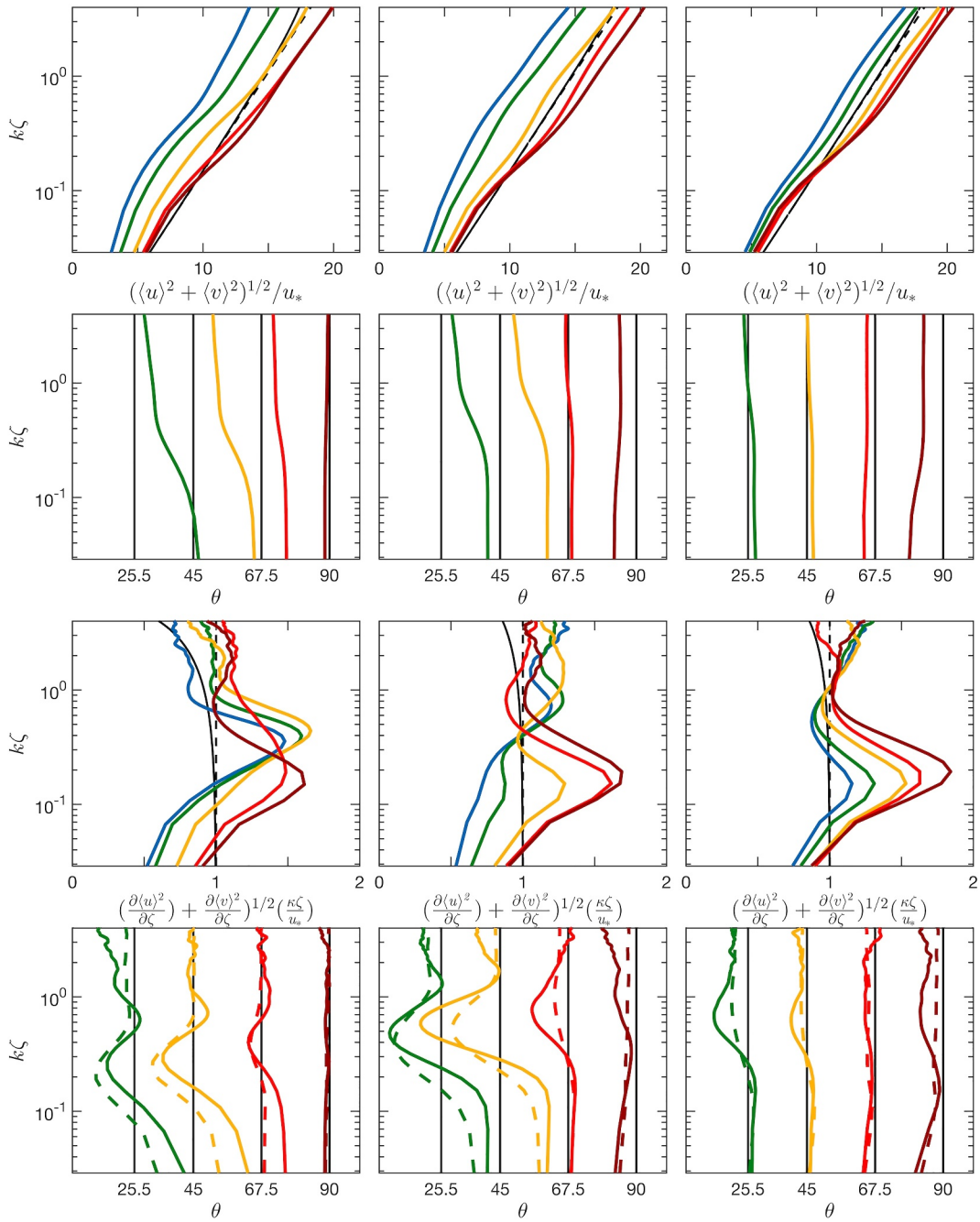

Figure 2. Normalized vertical profiles of horizontally averaged wind variables for $c/u_* = 1.37, 5.48, 10.95$ (left, middle, right columns). From top to bottom: mean wind magnitude, mean wind angle, mean wind shear magnitude, and mean wind shear angle (solid lines) with mean turbulence stress angle (dot-dashed lines). Results shown for $\theta = 0, 22.5, 45, 67.5, 90°$ (blue, green, orange, light red, dark red). Black lines show flat wall profiles (explained further in text).

$\theta > 22.5°$ for the high wave age. Husain et al. (2022a) found preliminary results of this drag reduction for $\theta > 45°$ under strongly forced conditions (the lowest wage age of 1.37), and this study demonstrates that the drag reduction occurs ubiquitously across all wave ages up to 10.95. It is particularly noteworthy that as θ approaches 90° the drag reduction becomes less dependent on the wave age and converges to around 0.3–0.45.

It is not straightforward to translate this reduction of the equivalent roughness length to the reduction of the drag coefficient, because the drag coefficient over the real ocean depends on a spectrum of waves. Nevertheless, if we

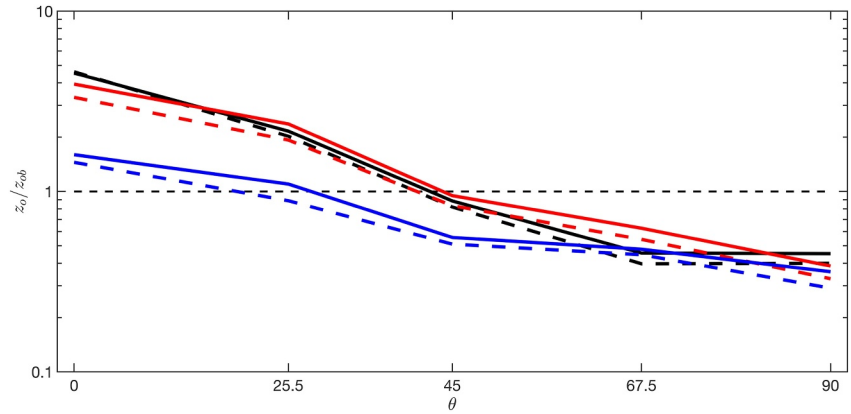

Figure 3. Roughness ratio z_o/z_{ob} plotted against misalignment angle θ for $c/u_* = 1.37$ (thick black lines), $c/u_* = 5.48$ (thick red lines), and $c/u_* = 10.95$ (thick blue lines). Dashed and solid lines show uncertainty of estimates explained further in text. Thin dashed black line shows value for flat wall case.

simply apply our result of the roughness reduction $z_o/z_{ob} = 0.3$ to a typical value of the drag coefficient 0.003 in high wind conditions, the drag coefficient is reduced by about 26% by the misaligned wave train. Furthermore, if we compare the aligned wave case ($\theta = 0°$) and the misaligned wave case ($\theta = 90°$) for $c/u_* = 1.37$, the equivalent roughness length decreases by a factor of about 0.1 by turning the wave direction, which is equivalent to about 42% reduction of the drag coefficient.

Zhou et al. (2022) report that the drag coefficient under tropical cyclones (wind speed 25–45 m/s) is almost independent of wind speed at around 0.0021, but it is significantly reduced as the misalignment angle θ between wind and dominant waves increases. The wave age values of the observations are mostly between 6 and 13. Using our LES results we may make rough estimation of how the drag coefficient decreases with increasing θ, if we assume that the drag coefficient for the aligned condition ($\theta = 0°$) is around 0.0021 and the observed dominant waves can be represented by a single wave train of a wave slope $ak = 0.27$ used in the simulations. The results are shown in Figure 4 and are compared with the observations. Our results are roughly consistent with the observed drag reduction of 20%–30% up to $\theta = 67.5°$. Our results overestimate the drag coefficient at larger misalignment angles but the errorbar of the observations is large. We do not compare our results with the shallow water observations by Potter et al. (2022) because they speculate that their observations are influenced by wave shoaling and fetch limitations. These effects are not accounted for in our LES simulations. Nevertheless, they also report drag coefficient reduction of up to 50% as θ approaches 90°, which is comparable to the drag reduction observed under tropical cyclones.

3.1.3. Wind Direction

Next we examine the misalignment between wind direction and wind stress direction (second row of Figure 2), which is another quantity of interest over misaligned surface waves. For the lowest wave age of $c/u_* = 1.37$, the wind direction significantly varies with height. The angle of the wind, measured counterclockwise from the wave direction, becomes much larger than the angle of the wind stress θ (solid black lines) toward the surface at $\theta = 22.5°$–45°, and to a less extent at $\theta = 67.5°$. As misalignment increases to $\theta = 90°$, the angle of the wind is nearly constant with height and is close to the angle of the wind stress. This is not surprising because the wave phase speed is relatively small (small wave age) and the wave train appears almost frozen and perpendicular for the wind above.

As the wave age increases to $c/u_* = 5.48$, the angle of the wind is less misaligned from the angle of the wind stress near the surface, but still relatively height dependent at $\theta = 22.5°$ and 45°. At $\theta = 67.5°$ the wind is nearly aligned with the wind stress. At $\theta = 90°$ the angle of the wind becomes less than the angle of the wind stress. This is likely because as the wave phase speed (wave age) increases, the wave phase speed becomes much larger than the along-wave component of far-field wind, that is, far-field wind blows increasingly

Table 1
Roughness Enhancement z_o/z_{ob}, Calculated at Lower Elevation

	$\theta = 0°$	$\theta = 22.5°$	$\theta = 45°$	$\theta = 67.5°$	$\theta = 90°$
$c/u_* = 1.37$, $k\zeta = 2$	4.53	2.16	0.89	0.46	0.45
$c/u_* = 5.48$, $k\zeta = 4$	3.93	2.37	0.95	0.63	0.39
$c/u_* = 10.95$, $k\zeta = 4$	1.57	1.07	0.56	0.48	0.36

Table 2
Roughness Enhancement z_o/z_{ob}, Calculated at Higher Elevation

	$\theta = 0$	$\theta = 22.5°$	$\theta = 45°$	$\theta = 67.5°$	$\theta = 90°$
$c/u_* = 1.37$, $k\zeta = 3$	4.61	2.02	0.82	0.40	0.40
$c/u_* = 5.48$, $k\zeta = 6$	3.33	1.93	0.83	0.54	0.33
$c/u_* = 10.95$, $k\zeta = 6$	1.43	0.89	0.51	0.45	0.30

backward relative to the moving wave. At $c/u_* = 10.95$, the angle of the wind is relatively constant with height. It is slightly larger than the angle of the wind stress at $\theta = 22.5°$ but becomes significantly less than the angle of the wind stress at $\theta = 90°$.

3.1.4. Wind Shear Profile

In order to better understand the enhancement of the far-field wind speed and the drag reduction, we next examine the vertical wind shear magnitude profile shown in the third row of Figure 2. When the shear is to the left (right) of the solid black line, the far-field wind speed magnitude decreases (increases) compared to the flat wall profile. The area integral of the shear is roughly proportional to the wind speed magnitude at the top (Hara & Sullivan, 2015).

Previous studies (Hara & Sullivan, 2015; Husain et al., 2019) show that when wind and waves are aligned and the wave age is small, the wind shear is modified in two different ways. First, the wind shear is reduced toward the surface where the turbulent stress is reduced and the wave-induced (pressure) stress is enhanced. Second, the wind shear is enhanced around $k\zeta = 0.3 - 0.5$ where the turbulent stress and the upward wave-coherent stress are enhanced due to intermittent flow separation. Since the former modification has a larger contribution to the overall wind profile, the far-field wind speed is reduced and the equivalent roughness and the drag coefficient increase due to the wave train. Husain et al. (2022a, 2022b) then show that these two wind shear modifications are weakened as the wave age increases or misalignment between wind and waves increases.

A new finding of this study is that there is a third kind of modification to the wind shear profile. As the misalignment angle θ increases and the two aforementioned modifications weaken, the wind shear is gradually enhanced around $k\zeta = 0.1 - 0.3$. This enhanced wind shear is mainly responsible for the overall increase of the far-field wind speed and the drag reduction. The results of $c/u_* = 1.37$ suggest that the shear enhancement around $k\zeta = 0.3 - 0.5$ due to flow separation slowly migrates down to $k\zeta = 0.1 - 0.3$ as θ increases. For $c/u_* = 10.95$ the two aforementioned modifications are weak and the only notable shear modification is the enhancement around $k\zeta = 0.1 - 0.3$. We will further investigate this wind shear enhancement by the misaligned waves in the following sections.

Lastly, we investigate the wind shear direction (bottom row of Figure 2). Similar to the wind speed direction, the angle of the wind shear also significantly varies with height at lower wave ages and smaller θ, and it is much larger than the angle of the wind stress (solid black lines) toward the surface. Unlike the angle of the wind speed, however, the angle of the wind shear becomes smaller than the angle of the wind stress at some height before it approaches the angle of the wind stress in the far-field.

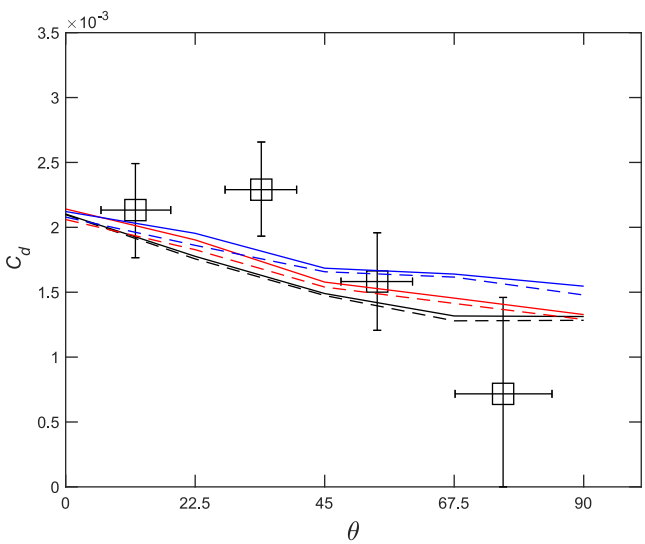

Figure 4. Drag coefficient C_d under tropical cyclones plotted against misalignment angle θ. Squares with errorbars are observational estimates reported by Zhou et al. (2022). The estimates based on the Large Eddy Simulation results (assuming $C_d = 0.0021$ at $\theta = 0°$) are shown for $c/u_* = 1.37$ (thick black lines), $c/u_* = 5.48$ (thick red lines), and $c/u_* = 10.95$ (thick blue lines). Dashed and solid lines show uncertainty of estimates explained further in text.

In common turbulent closure models the turbulent stress is set equal to the mean wind shear multiplied by the eddy viscosity, that is, the turbulent stress direction is assumed to be equal to the mean wind shear direction. It is therefore of interest to examine whether this assumption is valid for wind over misaligned waves. In the bottom row of Figure 2 the turbulent stress direction is shown by colored dot-dashed lines. In general, the vertical profile of the turbulent stress direction is quite similar to the wind shear direction profile. The misalignment between the two is not negligible but remains relatively small (mostly less than 10° or so).

3.2. Horizontally Averaged Wind Profiles Projected in Wind Stress Direction

In order to better examine the causes behind the enhanced wind shear and the drag reduction, we introduce a rotated horizontal coordinate $(\mathcal{X} - \mathcal{Y})$,

$$\mathcal{X} = x\cos(\theta) + y\sin(\theta) \tag{7}$$

$$\mathcal{Y} = -x\sin(\theta) + y\cos(\theta) \tag{8}$$

such that the along-wind ($\mathcal{X}$) and cross-wind ($\mathcal{Y}$) components of each wind variable can be investigated. We use the direction θ of the wind stress (and the applied pressure gradient $-\nabla p$) instead of the mean wind direction because the latter is height dependent and is difficult to use. The horizontal wind speed vector (u, v) is denoted as ($\mathcal{U}$, $\mathcal{V}$) in this rotated coordinate. From here on we refer to these variables as along-wind and cross-wind components.

3.2.1. Horizontally Averaged Wind Speed and Wind Shear

We show the wind speed and wind shear (the same results of Figure 2) in the rotated coordinate, that is, show the along-wind and cross-wind components instead of the magnitude and direction, in Figure 5. Although the cross-wind components are not negligibly small, the profiles of along-wind wind speed and along-wind wind shear in Figure 5 are very similar to those of wind speed magnitude and wind shear magnitude in Figure 2. Therefore, the new figure clearly suggests that the drag reduction by misaligned waves is mainly caused by the enhancement of the along-wind wind shear around $k\zeta = 0.1 - 0.3$.

3.2.2. Horizontally Averaged TKE Profiles

We examine the vertical profiles of the horizontally averaged TKE and its three components in Figure 6. The top row shows the total TKE $\left(\langle\overline{e}\rangle/u_*^2\right)$, and the second to fourth rows show the along-wind $\left(0.5\langle\overline{\mathcal{U}'\mathcal{U}'}\rangle/u_*^2\right)$, cross-wind $\left(0.5\langle\overline{\mathcal{V}'\mathcal{V}'}\rangle/u_*^2\right)$, and vertical $\left(0.5\langle\overline{w'w'}\rangle/u_*^2\right)$ TKE components, respectively.

One immediately notices that the total TKE profiles (top row) show quite similar patterns as those of the along-wind wind shear shown in the third row of Figure 5. In particular, the total TKE is also enhanced around $k\zeta = 0.3 - 0.5$ for $c/u_* = 1.37$ and small θ due to flow separation, and this enhancement disappears as the wave age and/or θ increases. Instead, the total TKE becomes enhanced around $k\zeta = 0.1 - 0.3$ (or slightly above) as θ increases. These wave-induced modification patterns are almost identical for the along-wind components of TKE (second row), and the modifications are weak for the cross-wind and vertical components (third and bottom rows).

3.2.3. Horizontally Averaged Energy Budget

The energy budget are examined for all cases in Figure 7. Following Hara and Sullivan (2015), Husain et al. (2022a), the energy budget in the mapped vertical coordinate (ζ) is obtained by combining the budget equations for the wave-fluctuation energy $\left(E^w = \frac{1}{2}\left(\tilde{\mathcal{U}}\tilde{\mathcal{U}} + \tilde{\mathcal{V}}\tilde{\mathcal{V}} + \tilde{w}\tilde{w}\right)\right)$ and the TKE $\left(\overline{e} = \frac{1}{2}\left(\overline{\mathcal{U}'\mathcal{U}'} + \overline{\mathcal{V}'\mathcal{V}'} + \overline{w'w'}\right)\right)$:

$$-\langle\tilde{\mathcal{U}}\frac{1}{J}\rangle\frac{\partial P}{\partial\mathcal{X}}\frac{\kappa\zeta}{u_*^3} + \langle\tau_{aw}^{tot}\rangle\frac{\partial\langle\mathcal{U}\rangle}{\partial\zeta}\frac{\kappa\zeta}{u_*^3} - \frac{\partial(F^w + F^t)}{\partial\zeta}\frac{\kappa\zeta}{u_*^3} - \left\langle\frac{1}{J}\epsilon\right\rangle\frac{\kappa\zeta}{u_*^3} = 0 \tag{9}$$

The first term arises due to the imposed pressure gradient and is negligible, the second term is the shear production term, the third term is the transport term where F^w and F^t are the vertical transport of E^w and $\overline{e}$ respectively, and the last term is the viscous dissipation. For a more comprehensive derivation of the energy budget equations refer to Hara and Sullivan (2015).

The dotted lines in the top panels of Figure 7 show that the sum of all four terms is close to zero, suggesting that the energy budget is reasonably satisfied by the LES. The shear production (bottom row) is equal to the along-wind wind shear multiplied by the linearly decreasing total along-wind stress. Therefore, it is practically identical to the along-wind wind shear shown in the third row of Figure 5 except near the top. This shear production is roughly balanced by the viscous dissipation (solid lines in the top row) because the contribution of the transport term (middle row) is relatively small. We observe the enhanced viscous dissipation around $k\zeta = 0.3 - 0.5$ and reduced viscous dissipation further below for $c/u_* = 1.37$ and small θ. These signatures disappear as the wave age or θ increases. Instead, the enhancement of the viscous dissipation appears around $k\zeta = 0.1 - 0.3$ as θ increases.

In summary, the observed modifications (enhancement or reduction) of the along-wind wind shear is practically identical to those of the shear production and is very similar to those of the viscous dissipation. The observed shear enhancement is also well correlated with the enhancement of the TKE (or the along-wind component of the TKE). The remaining question is why the shear production, the viscous dissipation and the TKE are all enhanced around $k\zeta = 0.1 - 0.3$ as θ increases. To address this question, we examine the momentum budget next.

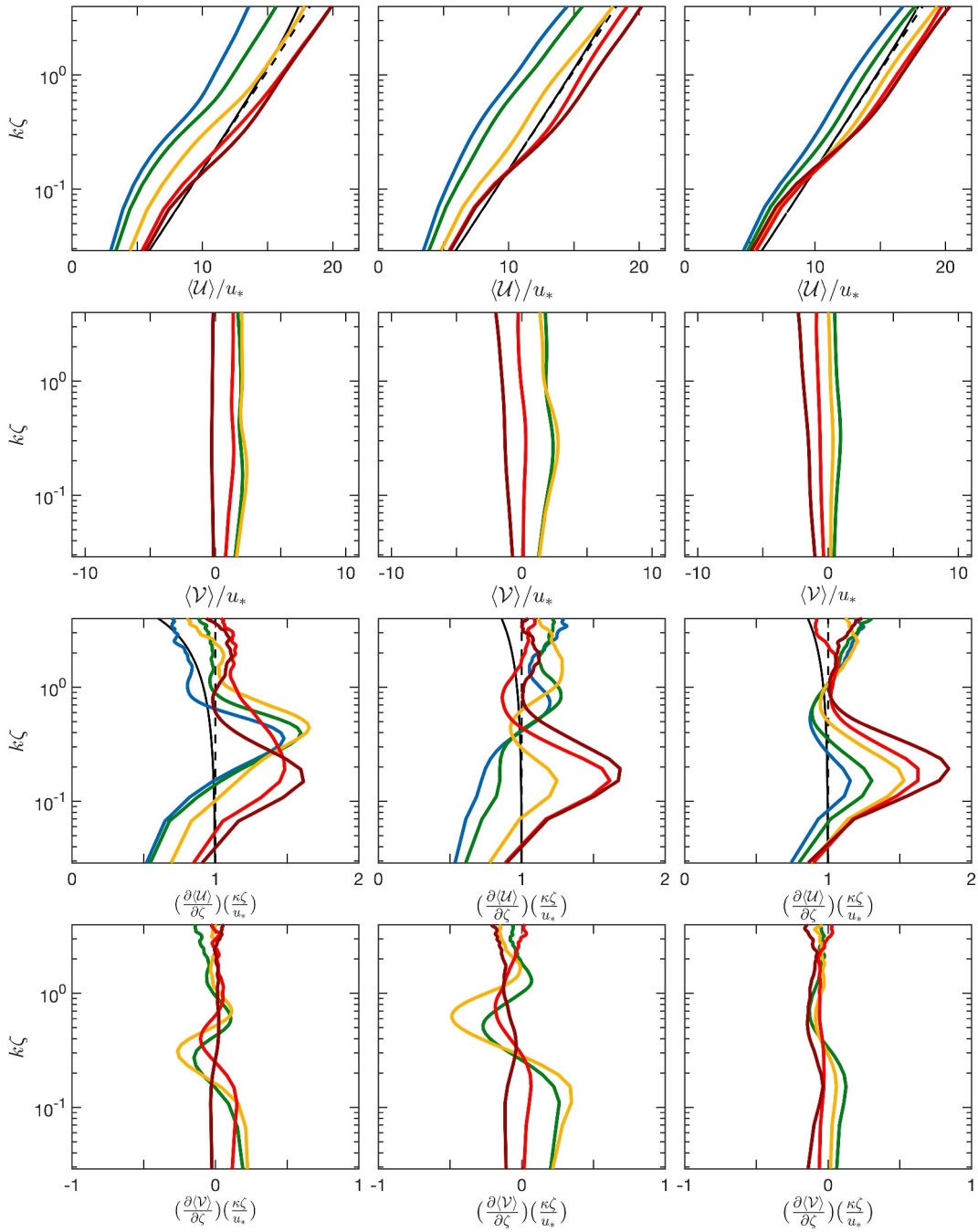

Figure 5. Vertical profiles of horizontally averaged wind variables in rotated coordinates for $c/u_* = 1.37, 5.48, 10.95$ (left, middle, right columns). From top to bottom: along-wind wind speed ($\langle \mathcal{U} \rangle / u_*$), cross-wind wind speed ($\langle \mathcal{V} \rangle / u_*$), along-wind wind shear $\left(\frac{\partial \langle \mathcal{U} \rangle}{\partial \zeta} \frac{\kappa}{u_*}\right)$, and cross-wind wind shear $\left(\frac{\partial \langle \mathcal{V} \rangle}{\partial \zeta} \frac{\kappa}{u_*}\right)$. Results shown for $\theta = 0, 22.5, 45, 67.5, 90°$ (blue, green, orange, light red, dark red). Black lines show flat wall profiles.

3.2.4. Horizontally Averaged Momentum Budget

For the cases of waves aligned with wind ($\theta = 0$) Hara and Sullivan (2015) and Husain et al. (2022b) show that the enhancement/reduction of the viscous dissipation rate is closely correlated with the enhancement/reduction of the turbulent stress magnitude, which is caused by the upward/downward wave-induced stress. Therefore, it is of interest to examine whether the observed enhanced viscous dissipation around $k\zeta = 0.1 - 0.3$ for large misalignment θ is also correlated with the enhanced turbulent stress magnitude.

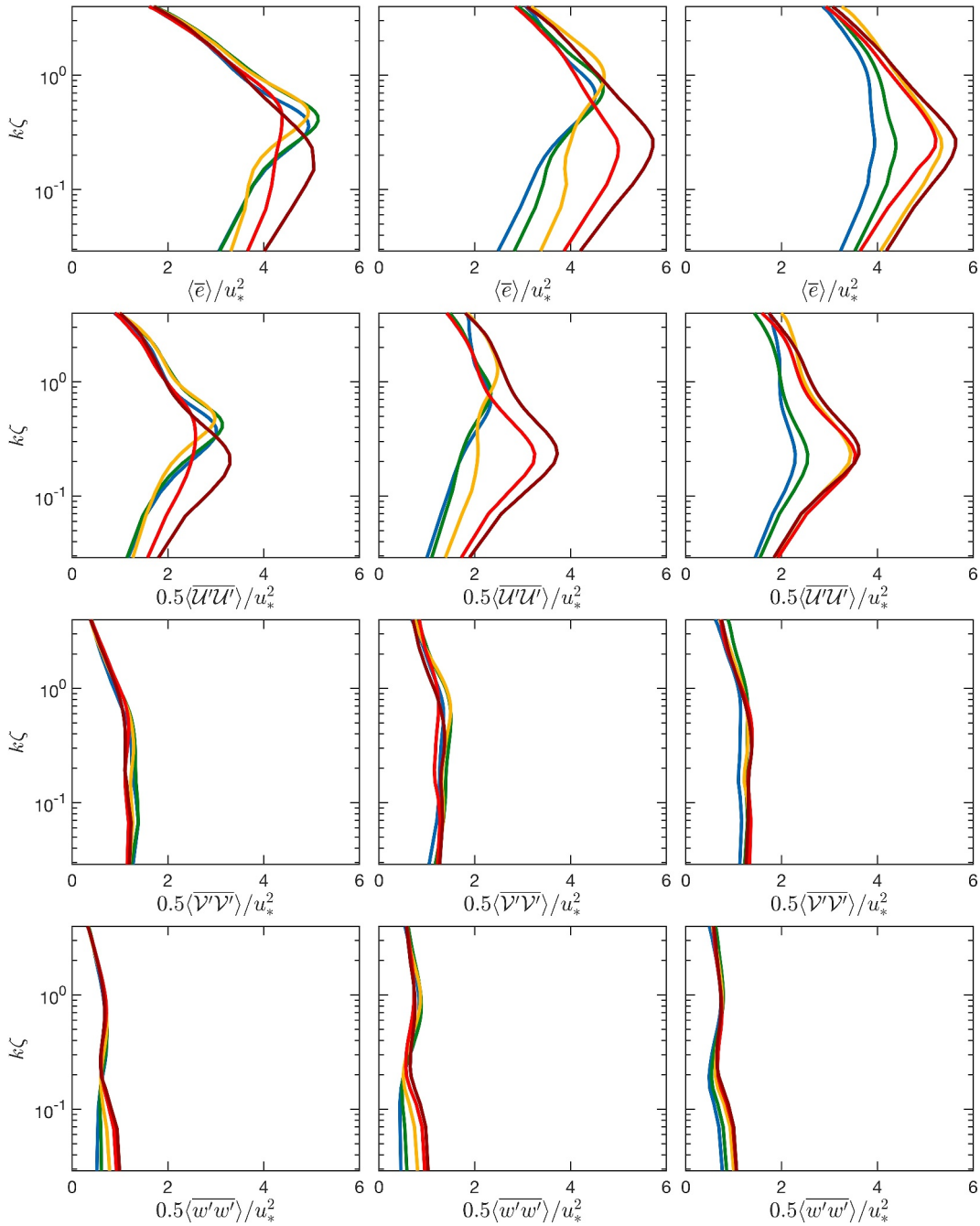

Figure 6. Normalized vertical profiles of horizontally averaged turbulent kinetic energy (TKE) for $c/u_* = 1.37, 5.48, 10.95$ (left, middle, right columns). From top to bottom: total TKE magnitude $\left(\langle\overline{e}\rangle/u_*^2\right)$, along-wind component $\left(0.5\langle\overline{\mathcal{U}'\mathcal{U}'}\rangle/\left(u_*^2\right)\right)$, cross-wind component $\left(0.5\langle\overline{\mathcal{V}'\mathcal{V}'}\rangle/\left(u_*^2\right)\right)$, and vertical component $\left(0.5\langle\overline{w'w'}\rangle/\left(u_*^2\right)\right)$. Results shown for $\theta = 0, 22.5, 45, 67.5, 90°$ (blue, green, orange, light red, dark red).

In Husain et al. (2022a), the momentum budget is analyzed in both the along-wave and cross-wave directions separately. Here, we instead focus on the momentum budget in the along-wind ($\mathcal{X}$) direction, which is summarized as

$$\frac{\langle\tau_{aw}^{w}\rangle}{u_*^2}+\frac{\langle\tau_{aw}^{p}\rangle}{u_*^2}+\frac{\langle\tau_{aw}^{t}\rangle}{u_*^2}=\frac{\langle\tau_{aw}^{tot}\rangle}{u_*^2}=-\frac{\frac{\partial p}{\partial\mathcal{X}}\zeta}{u_*^2}-1 \tag{10}$$

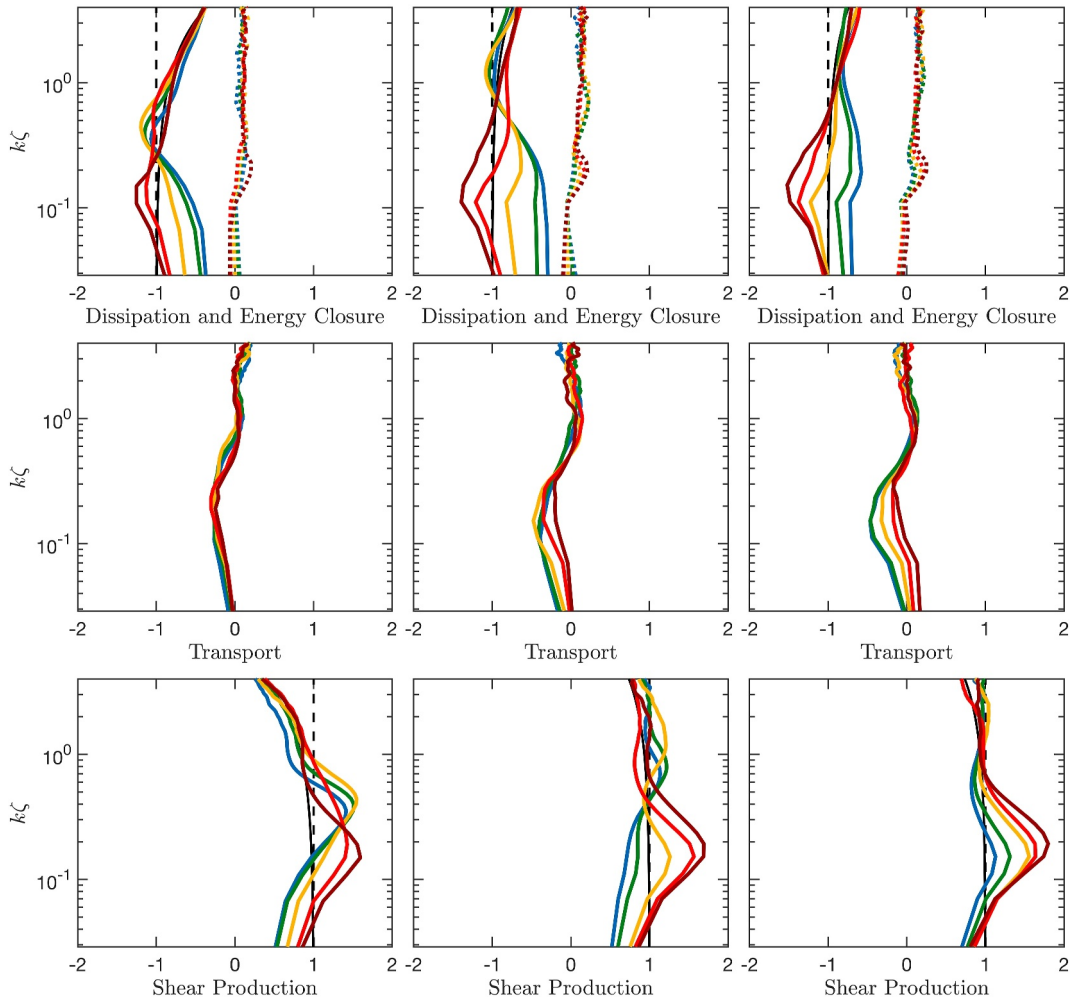

Figure 7. Normalized vertical profiles of horizontally averaged energy budget terms for $c/u_* = 1.37, 5.48, 10.95$ (left, middle, right columns) as explained in text. From top to bottom: dissipation term (solid lines) and sum of all energy terms (dotted lines), transport term, and shear production term. Results shown for $\theta = 0, 22.5, 45, 67.5, 90°$ (blue, green, orange, light red, dark red). Black lines show flat wall profiles.

The first term on the left is the wave-coherent stress $\langle \tau^w_{aw} \rangle = \langle \tilde{\mathcal{U}}\tilde{W} \rangle$ and the second term represents the pressure (form) stress $\langle \tau^p_{aw} \rangle = \langle \frac{1}{\overline{\rho}} \overline{p} \frac{\partial \zeta}{\partial x} \rangle$. The wave-induced stress comprises these two terms. The third term represents the turbulent stress $\langle \tau^t_{aw} \rangle = \langle \mathcal{U}'W' \rangle$, which is further composed of the resolved turbulent stress and the SGS parameterization. The right hand side represents the linearly varying stress profile from the imposed horizontal pressure gradient.

We show the vertical profiles of the horizontally averaged momentum budget in the along-wind direction in Figure 8. The top row shows that the LES has converged to satisfy the momentum budget reasonably well. Similar to Husain et al. (2022a), our results of $c/u_* = 1.37$ and small θ show large enhancement of the pressure stress (negative downward flux) toward the surface and large enhancement of the wave coherent stress (positive upward flux) around $k\zeta = 0.3 - 0.5$ due to intermittent flow separation events. Since the total wind stress is constrained, the turbulent stress magnitude is significantly reduced toward the surface and is enhanced (becomes larger than the total wind stress magnitude) around $k\zeta = 0.3 - 0.5$. These signatures are well correlated with the enhancement/reduction of viscous dissipation, shear production, and TKE. These modifications gradually disappear as the wave age and/or θ increases.

For all wave ages, as θ approaches 90°, both the pressure stress and the wave-coherent stress become small and the turbulent stress becomes almost the same as the total stress, that is, becomes unaffected by the waves. Therefore,

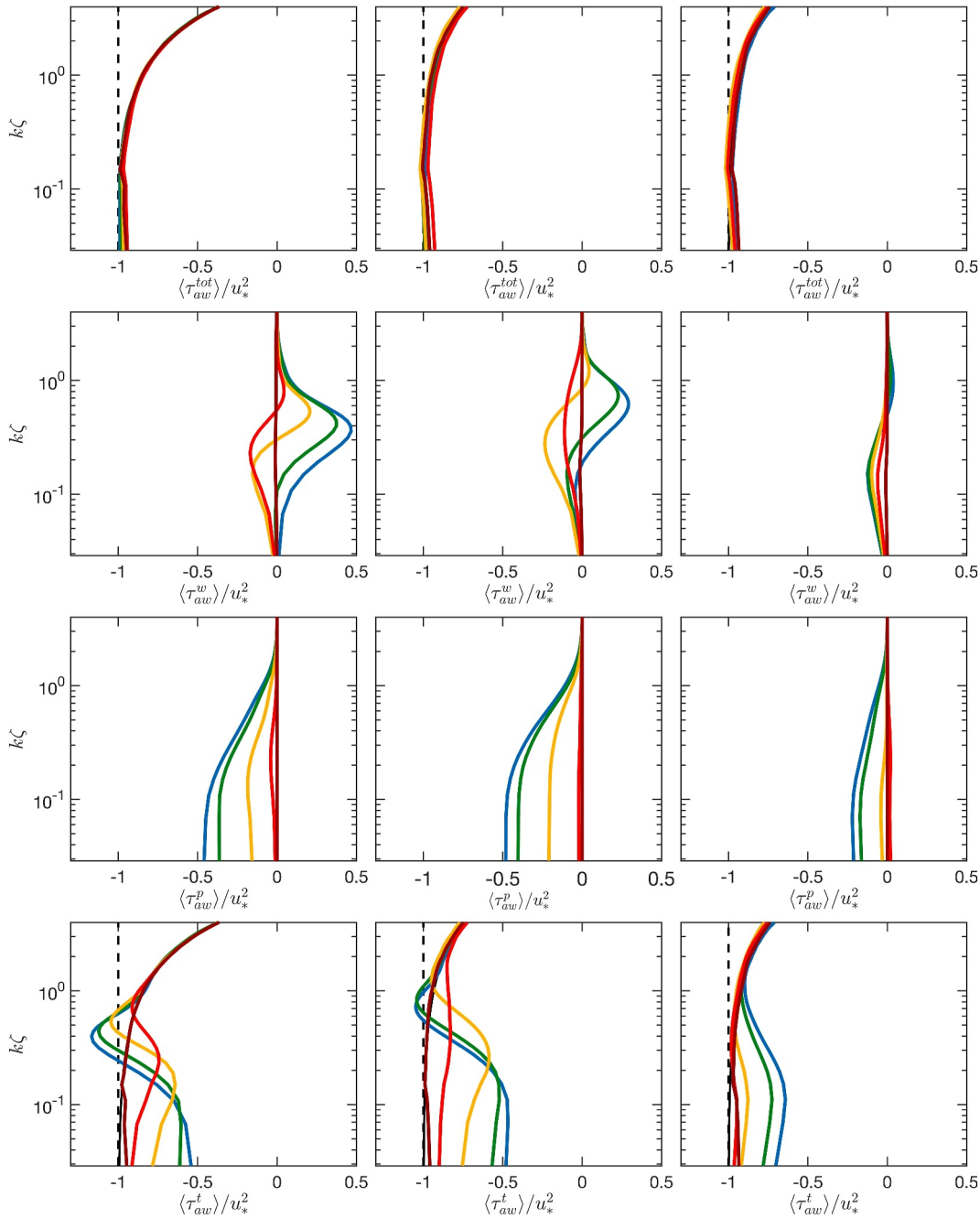

Figure 8. Normalized vertical profiles of horizontally averaged along-wind momentum budget terms for $c/u_* = 1.37$, 5.48, 10.95 (left, middle, right columns) as explained in text. From top to bottom: total wind stress ($\langle\tau_{aw}^{tot}\rangle$), wave-coherent stress ($\langle\tau_{aw}^{w}\rangle$), pressure stress ($\langle\tau_{aw}^{p}\rangle$), and turbulence stress ($\langle\tau_{aw}^{t}\rangle$). Results shown for $\theta = 0$, 22.5, 45, 67.5, 90° (blue, green, orange, light red, dark red). Black lines show flat wall profiles.

the previously observed enhancement of the along-wind wind shear around $k\zeta = 0.1 - 0.3$ (which is responsible for the drag reduction), as well as the enhancement of the viscous dissipation and the TKE, is uncorrelated with the turbulent stress, that is, it is very different from the wave-induced modulations in the wind-wave aligned case.

3.3. 2D Flow Fields

In this section we investigate 2D phase averaged flow fields as well as 2D instantaneous turbulent vorticity fields to better understand the impact of misaligned surface waves at different wave phases (from crest to trough to next

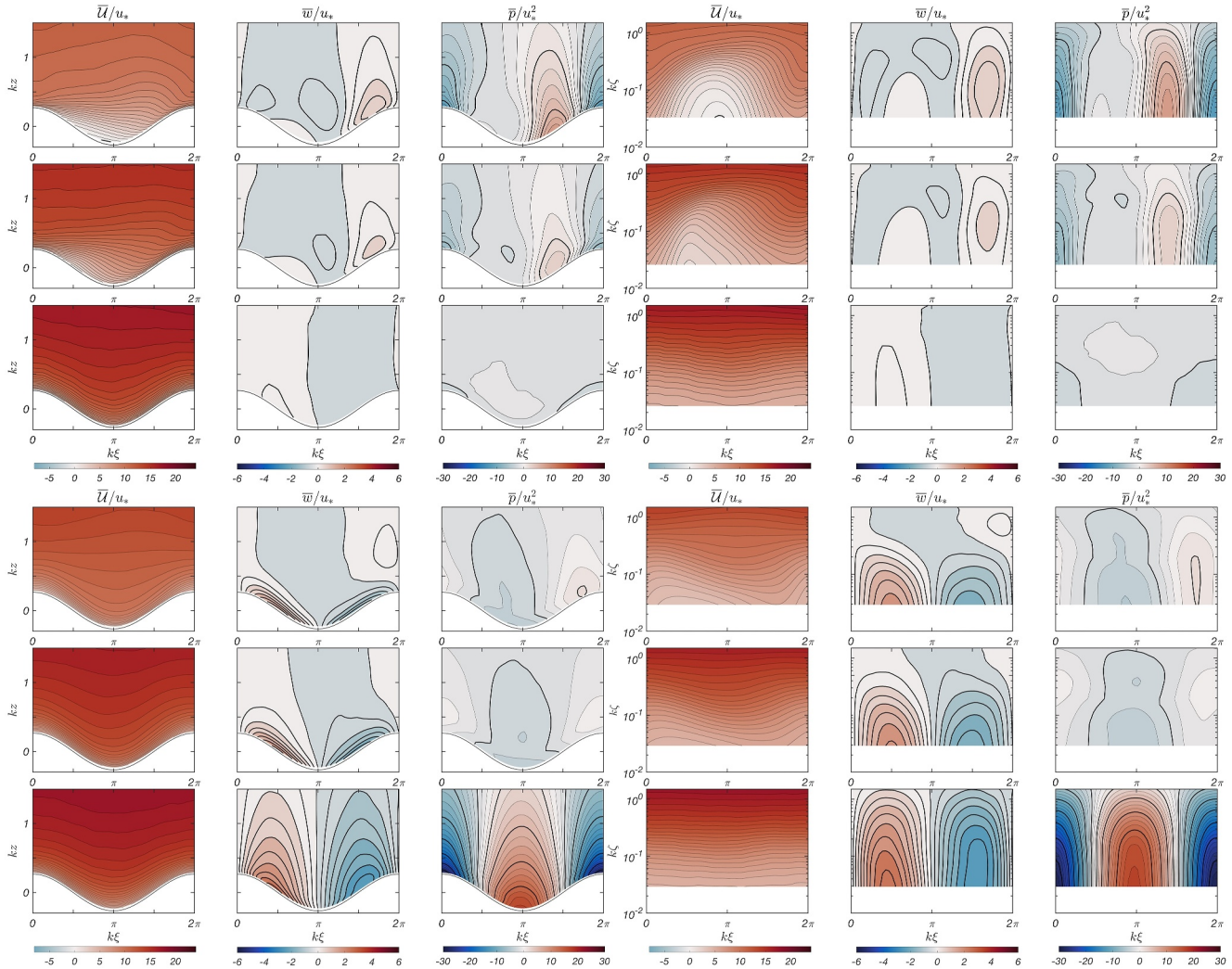

Figure 9. Normalized phase-averaged flow fields in the physical ($\xi - z$) coordinate (left three panels) and mapped ($\xi - \zeta$) coordinate (right three panels) for $c/u_* = 1.37$ (1st–3rd rows) and $c/u_* = 10.95$ (4th–6th rows). From left to right: along-wind velocity $\left(\overline{U}/u_*\right)$, vertical velocity $\left(\overline{w}/u_*\right)$, and pressure $\left(\overline{p}/u_*^2\right)$. Results shown for $\theta = 0$, 45, 90° (1st/4th, 2nd/5th, 3rd/6th rows).

crest). In Figures 9 and 10 the phase averaged results are shown for $c/u_* = 1.37$ (1st–3rd rows) and $c/u_* = 10.95$ (4th–6th rows) and for $\theta = 0°$ (1st and 4th rows), 45° (2nd and 5th rows), and 90° (3rd and 6th rows). The left three columns are plotted in the physical ($\xi - z$) coordinates. The same quantities are plotted in the mapped ($\xi - \zeta$) coordinates in the right three columns with the vertical axis in log scale so that the results near the surface can be seen more clearly. All results are normalized by u_* and k.

3.3.1. Phase Averaged Velocities and Pressure

Let us first examine the along-wind $\left(\overline{U}/u_*\right)$ velocity fields, shown in the 1st and 4th columns in Figure 9 (The cross-wind velocity is quite weak and not shown.) As discussed in Husain et al. (2022b) the along-wind velocity for $c/u_* = 1.37$ and $\theta = 0°$ (top row) clearly shows signature of flow separation downstream of the crest, and this signature weakens as the wave age or θ increases. At $\theta = 90°$ the along-wind flow becomes quite smooth and becomes almost parallel (independent of phase) in the mapped coordinate (4th column, 3rd and 6th rows). They also show clear enhancement of the mean shear (closer contours) around $k\zeta = 0.1 - 0.3$ at all wave phases (Note that the distance between the successive contours is uniform for the logarithmic wind profile over a flat surface).

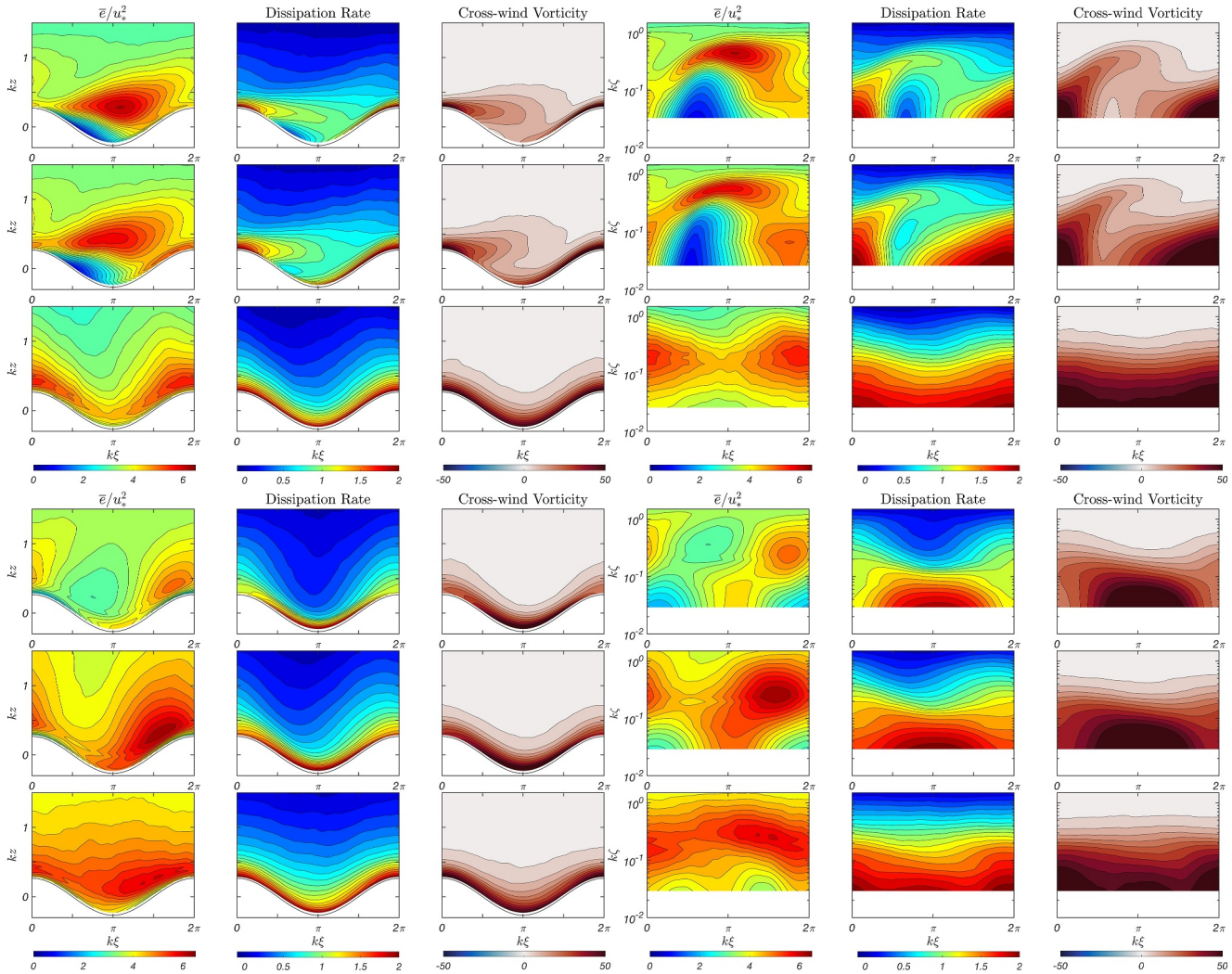

Figure 10. Normalized phase-averaged flow fields in the physical ($\xi - z$) coordinate (left three panels) and mapped ($\xi - \zeta$) coordinate (right three panels) for $c/u_* = 1.37$ (1st–3rd rows) and $c/u_* = 10.95$ (4th–6th rows). From left to right: turbulent kinetic energy $\left(\overline{e}/u_*^2\right)$, dissipation rate $\left(\epsilon/\left(ku_*^3\right)\right)$, and cross-wind vorticity $\left(\overline{\omega}_{cw}/\left(ku_*^2\right)\right)$. Results shown for $\theta = 0, 45, 90°$ (1st/4th, 2nd/5th, 3rd/6th rows).

The near surface vertical velocity $\left(\overline{w}/u_*\right)$, shown in the 2nd and 5th columns, is mainly determined by how wind blows relative to the moving wave. When the wind velocity in the wave direction (x direction) is larger (smaller) than the wave phase speed, the vertical velocity becomes positive (negative) in the windward side and negative (positive) in the lee side of the wave crest. The $\overline{w}/u_*$ fields in Figure 9 show that the along-wave component of the near surface wind speed (relative to the moving wave) decreases from top to bottom. It is positive at the top two rows ($\theta = 0, 45°$), is almost zero in the third row ($\theta = 90°$), and becomes negative in the bottom three rows (all θ for $c/u_* = 10.95$). These flow fields likely control the behavior of the enhanced TKE as discussed below.

Next, we examine the pressure field $\left(\overline{p}/u_*^2\right)$, shown in the 3rd and 6th columns. As discussed by Husain et al. (2022b), for $c/u_* = 1.37$ and $\theta = 0°$ (top row) the near surface pressure is high along the leeward face of the wave where the separated flow reattaches, and this signature decreases as c/u_* or θ increases (second and fourth rows). The wave-induced modulation of pressure is very weak for $c/u_* = 1.37$ and $\theta = 90°$ (third row). However, it becomes very strong for $c/u_* = 10.95$ and $\theta = 90°$, where the large pressure modulation is almost in phase with the wave elevation and does not contribute to the wave form drag or the wave growth/decay, as discussed in Section 3.4. This nearly in phase signature resembles those observed in opposing wind-wave cases (see bottom panels of Figure 2 in Husain et al., 2022b) and appears to be a robust feature when the negative near-surface along-wave (x) velocity (relative to the moving wave) and the resulting $\overline{w}$ becomes sufficiently strong.

3.3.2. Phase Averaged TKE, Dissipation Rate, and Vorticity

We next examine the TKE, dissipation rate, and cross-wind vorticity fields in Figure 10. Similar to Husain et al. (2022a) we see evidence of flow detachment from the crest for $c/u_* = 1.37$ at $\theta = 0, 45°$ (top and second rows) with regions of enhanced TKE, dissipation rate, and vorticity extending downstream from the wave crest. As misalignment increases to $\theta = 90°$ (third row), the flow separation signature disappears but a new region of enhanced TKE appears above the wave crest around $k\zeta = 0.1 - 0.4$.

A similar signature of enhanced TKE around $k\zeta = 0.1 - 0.4$ is observed for $c/u_* = 10.95$ and $\theta = 45, 90°$. Its peak location is slightly shifted to the left from the wave crest at $\theta = 45°$ (fifth row) and migrates further to the left as θ increases to 90° (bottom row). At the same time the enhancement region becomes more diffused horizontally. These patterns suggest that this enhanced TKE region around $k\zeta = 0.1 - 0.4$ originates above the wave crest, and is advected to the left and horizontally diffused by the negative along-wave velocity (relative to the moving wave), which becomes stronger as θ increases as discussed earlier.

It is more difficult to see the wave-induced modulations of the dissipation rate and the cross-wind vorticity without the flow separation effects (3rd to bottom rows), since these variables rapidly increase toward the surface even without the wave. Both variables seem to be enhanced just above the wave trough for $c/u_* = 10.95$ and $\theta = 0$, 45° (4th and 5th rows), but are more evenly distributed with wave phase for $\theta = 90°$ (3rd and bottom rows).

3.3.3. Turbulent Vorticity Fields

In order to further examine the turbulent eddies that contribute to the enhanced TKE, we plot instantaneous turbulent cross-wind vorticity (ω'_{cw}/ku_*) fields in Figures 11 and 12. The turbulent vorticity is calculated at and above the second LES grid level by subtracting the phase-averaged velocities from the instantaneous velocities, which differs from methods used in Husain et al. (2022a, 2022b). For the aligned case (top row) we examine the vorticity fields $\omega'_{cw} = \omega'_y$ along the wave. For $\theta = 90°$, we examine the vorticity fields along both the crest (middle row) and trough of the wave (bottom row) where $\omega'_{cw} = -\omega'_x$. All results are plotted as a function of the height above the wavy surface $(z - h\,(x, t))$.

We see further evidence of airflow separation in the low wave age aligned case (top panel of Figure 11) with stretched vortices extending high above the crest. It is immediately clear that the vorticity is less enhanced for the high wave age aligned case (top panel of Figure 12). While turbulent vorticity fields and TKE are not the same, we do see similar patterns of enhancement due to misaligned waves ($\theta = 90°$) between the two. For the low wave age case, the vorticity along the crest (middle panel of Figure 11) is clearly enhanced around $k\,(z - h) = 0.1 - 0.4$, which is roughly consistent with the enhanced TKE at around $k\zeta = 0.1 - 0.4$ discussed earlier. The vorticity enhancement is not as clear along the trough (bottom panel of Figure 11). For the high wave age case (Figure 12), the vorticity along the trough (bottom panel) is similarly enhanced as the crest (middle panel), matching the TKE pattern we saw in Figure 10.

Based on the analyses of the LES results in this and previous sections, we may summarize our findings regarding the mechanism of the drag reduction as follows.

1. Our horizontally averaged (1D) analysis of wind over a misaligned wave train suggests that the drag reduction by the misaligned wave is mainly caused by the enhanced along-wind wind shear around $k\zeta = 0.1 - 0.3$. The TKE and the dissipation rate are also enhanced around the same height. Although the wave-induced modulations of wind shear, TKE, and dissipation rate are strongly correlated with the wave-induced modulation of the turbulent stress in the wind-wave aligned cases ($\theta = 0°$), they are not correlated with the turbulent stress modulation (which is very weak) in the misaligned cases.
2. Our 2D flow field analysis of wind over a misaligned wave train suggests that the enhanced TKE region appears first above the wave crest around $k\zeta = 0.1 - 0.4$, possibly resulting from interaction between the wave crest and the along-crest (cross-wave) wind just above. This enhanced TKE region appears to be slowly advected by the along-wave component of the wind and horizontally diffused. This 2D TKE signature is consistent with the enhanced TKE signature in the 1D analysis, as well as consistent with the instantaneous turbulent vorticity fields. We may speculate that this enhanced TKE is related to the enhanced along-wind wind shear and the resulting drag reduction.

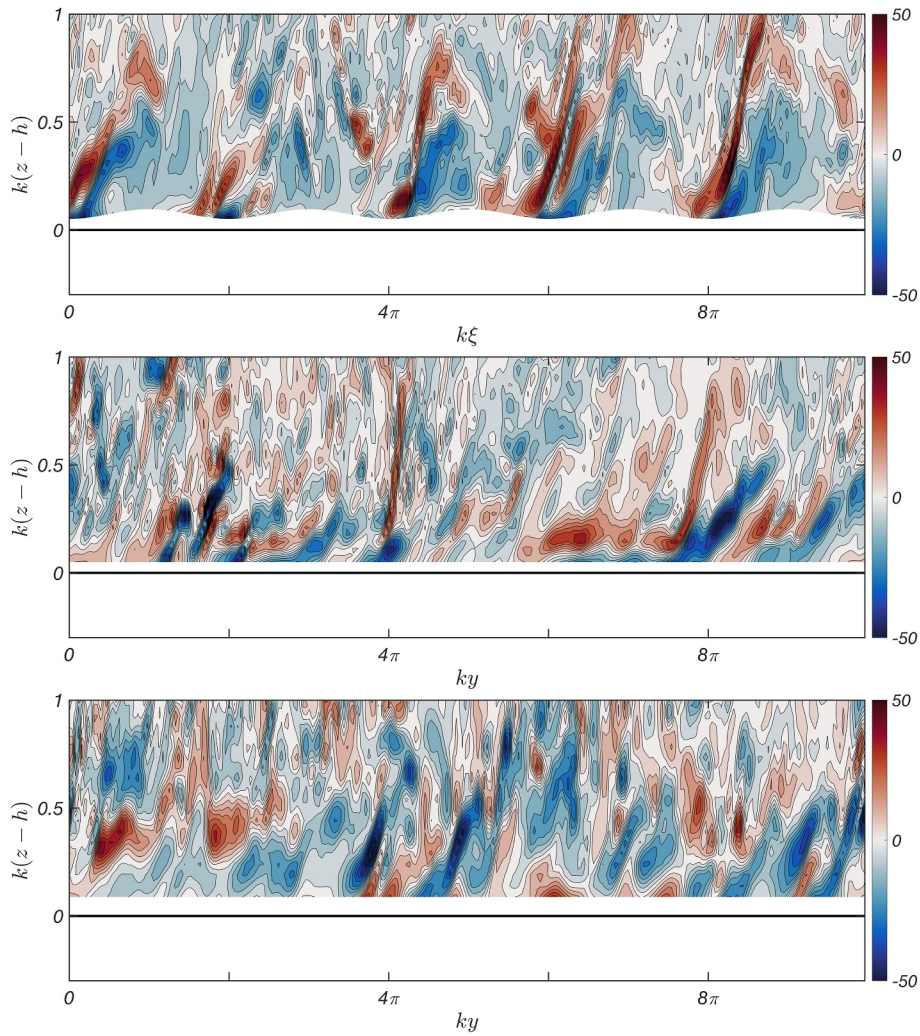

Figure 11. Normalized turbulent cross-wind vorticity ($\omega'_{cw}/(ku_*)$) fields for $c/u_* = 1.37$ for $\theta = 0°$ (top panel) and $\theta = 90°$ (bottom two panels). For aligned case (top row) vorticity is shown along the wave and for $\theta = 90°$ vorticity is shown along the crest of the wave (middle row) and trough of the wave (bottom row). Black lines represent mean water surface.

3.4. Surface Stress and Wave Growth/Decay Rate

In order to calculate the energy flux (EF) into the waves, both the normal stress and tangential stress (in the wave direction x) must be considered as explained in Hara and Sullivan (2015) and Husain et al. (2019, 2022b). The wave growth/decay rate β is then found by dividing EF by the wave energy, and is commonly expressed as follows:

$$\beta = c_\beta \left(\frac{u_*}{c}\right)^2 \frac{\rho_a}{\rho_w}\omega \tag{11}$$

where c_β is a non-dimensional coefficient. We examine the components of the coefficient c_β from the tangential turbulent stress only ($c_{\beta t}$), the normal turbulent stress only ($c_{\beta n}$), and pressure only ($c_{\beta p}$), as well as the total ($c_{\beta tot}$) from the total energy flux. These values are summarized in Tables 3–5 and Figure 13, where the results of $c_{\beta tot}$, $c_{\beta p}$, and $c_{\beta p} + c_{\beta n}$ are plotted by large red dots, small red dots, and red stars, respectively. Note that the tangential stress contributes to the energy flux (wave growth/decay) but does not contribute to the wave form drag. Therefore, the total normal stress contribution, $c_{\beta p} + c_{\beta n}$, can be interpreted as a measure of the wave form drag.

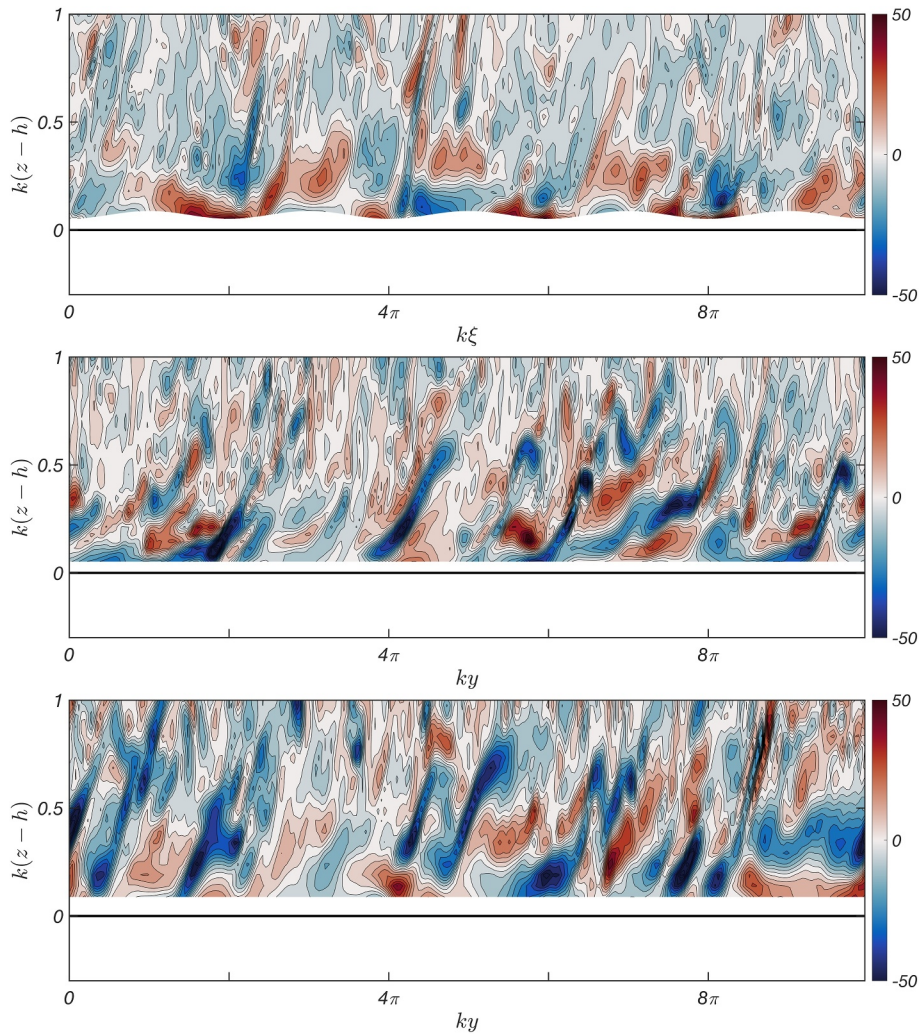

Figure 12. Same as Figure 11 for $c/u_* = 10.95$.

Let us examine the pressure, the normal turbulent stress, and the tangential turbulent stress (in the x direction) along the wave surface shown in Figure 14. As discussed earlier, there is a strong positive peak of the surface pressure in the windward side of the crest for $c/u_* = 1.37$ at $\theta = 0°$, which is mainly responsible for the large wave growth rate and the wave form drag. The tangential stress shows a negative peak near the wave crest and contributes to the wave growth, as shown in the left panel of Figure 13. These features become weaker as θ increases to 45°, and at $\theta = 90°$ both the total normal stress and the tangential stress are near zero. The wave growth coefficients become close to zero.

For $c/u_* = 10.95$ at $\theta = 0°$, the normal stress weakly contributes to positive wave growth and wave form drag. However, the tangential stress now shows a negative peak near the wave trough and significantly reduces the wave growth rate (right panel of Figure 13). As θ increases to 90°, the pressure modulation becomes very strong and is negative near the crest and positive near the trough of the wave. Since it is almost in phase with the wave elevation and out of phase with the vertical wave orbital velocity, its contribution to the wave decay is modest. The tangential stress exhibits the opposite behavior with a positive peak near the crest and a negative peak near the trough, and its contribution to the wave decay is as large as the normal total stress contribution.

Table 3
Wave Growth/Decay Coefficient at $c/u_* = 1.37$

	$\theta = 0$	$\theta = 22.5°$	$\theta = 45°$	$\theta = 67.5°$	$\theta = 90°$
$c_{\beta t}$	2.73	2.63	1.92	0.57	−0.24
$c_{\beta n}$	1.54	2.12	3.17	3.02	0.05
$c_{\beta p}$	13.23	11.36	6.40	0.83	−0.84
$c_{\beta tot}$	17.50	16.11	11.49	4.41	−1.03

Lastly, we examine whether the existing parameterizations of c_β predict the same dependence on the misalignment angle θ as our LES results. The growth

Table 4
Wave Growth/Decay Coefficient at $c/u_* = 5.48$

	$\theta = 0$	$\theta = 22.5°$	$\theta = 45°$	$\theta = 67.5°$	$\theta = 90°$
$c_{\beta t}$	0.10	−0.13	−0.47	−0.84	−1.31
$c_{\beta n}$	1.32	1.28	0.90	0.14	−0.28
$c_{\beta p}$	13.94	12.67	8.59	1.53	−1.80
$c_{\beta tot}$	15.37	13.83	9.02	0.84	−3.40

rate parameterization based on the wind stress normally assumes that the growth rate decreases like $\cos\theta$ or $\cos^2\theta$ as θ increases. In Figure 13 the dependencies of $\cos\theta$ and $\cos^2\theta$ of $c_{\beta tot}$ are shown by dashed and dotted lines. We also test the growth rate parameterization employed by Donelan et al. (2012), Reichl et al. (2014) shown by a solid line, which is based on the wind speed magnitude $u_{\lambda/2}$ and direction θ_w at a half wave length height (solid line), $A\,(u_{\lambda/2}\cos(\theta_w) - c)|u_{\lambda/2}\cos(\theta_w) - c|$, where $A = 0.11$ for $u_{\lambda/2}\cos(\theta_w) > c$ and $A = 0.01$ for $0 < u_{\lambda/2}\cos(\theta_w) < c$.

The result of $c/u_* = 1.37$ (left panel) is similar to the result of Husain et al. (2022a) with the addition of the $\theta = 90°$ case. All three parameterizations seem to capture the decrease of the growth rate reasonably well. For $c/u_* = 5.48$ (middle panel) the $\cos\theta$ dependence significantly overestimates the growth rate at large θ, but the other two parameterizations are still reasonable. For $c/u_* = 10.95$ (right panel) all parameterizations fail to capture the large wave decay rate and the large negative form drag at $\theta = 90°$. Although the wind speed based parameterization correctly predicts negative growth rate and negative form drag at large θ, their magnitude is significantly underestimated.

4. Concluding Remarks

The previous LES study of wind over a misaligned wave train by Husain et al. (2022a) at wave age 1.37 (a strongly forced condition) has shown that the equivalent roughness length and the drag coefficient decrease, that is, the wave train makes the surface smoother, when the misalignment angle θ (between the wind stress direction and the wave propagation direction) exceeds about 45°. Recent field observational studies suggest that the drag coefficient may be significantly reduced when the dominant surface waves are significantly misaligned from wind. Such conditions are common under tropical cyclones (where wind changes rapidly) or in coastal waters (where waves are refracted by the depth change). These observations, however, correspond to much larger wave ages than 1.37 studied by Husain et al. (2022a).

Motivated by these recent observations, this study has extended the study of Husain et al. (2022a) by performing simulations at three different wave ages from 1.37 to 10.95 and with five different misalignment angles (θ) from 0 to 90°. The highest wave age of 10.95 has been chosen because it corresponds to a typical wave age of misaligned dominant waves under tropical cyclone winds. At wave ages 1.37 and 5.48 the equivalent roughness length and the drag coefficient become less than the (background) flat surface values when θ exceeds about 45°. The drag reduction occurs at smaller misalignment angles, roughly above 22.5°, at wave age 10.95. Therefore, this study has demonstrated that the drag reduction due to misaligned waves occurs ubiquitously over a wide range of wave age, including typical conditions of misaligned dominant waves under tropical cyclones.

Our 1D (horizontally averaged) analysis suggests that the drag reduction is mainly caused by the enhanced along-wind wind shear around $k\zeta = 0.1 - 0.3$ above the wavy surface. The TKE and the viscous dissipation rate are also enhanced around the same height. Although the wave-induced modulations of the wind shear, TKE, and dissipation rate are strongly correlated with the wave-modulated turbulent stress in the wind-wave aligned case, they are not correlated with the turbulent stress in the misaligned cases. This finding suggests that the existing turbulence closure models based on the enhanced/reduced turbulent stress, which work well for wind-wave aligned cases, are not applicable for misaligned cases; they would fail to predict the enhanced dissipation and enhanced wind shear due to misaligned waves.

Our 2D flow analysis suggests that the enhanced TKE region in the misaligned case originates above the wave crest, possibly due to interaction between the wave crest and the along-crest wind above. The enhanced TKE region slowly migrates and is horizontally diffused. We may speculate that this enhanced TKE may be related to the enhanced mean wind shear and the drag reduction. The wave growth rate and the wave form drag decreases as θ increases for $c/u_* = 1.37$ and 5.48 and is roughly consistent with the existing growth rate parameterizations. However, they become significantly negative at $\theta = 90°$ for $c/u_* = 10.95$, which the existing parameterizations fail to predict.

Table 5
Wave Growth/Decay Coefficient at $c/u_* = 10.95$

	$\theta = 0$	$\theta = 22.5°$	$\theta = 45°$	$\theta = 67.5°$	$\theta = 90°$
$c_{\beta t}$	−2.47	−2.49	−2.49	−2.68	−3.68
$c_{\beta n}$	−0.07	−0.23	−0.33	−0.50	−0.56
$c_{\beta p}$	7.49	5.10	1.30	−1.55	−3.94
$c_{\beta tot}$	4.96	2.38	−1.52	−4.73	−8.19

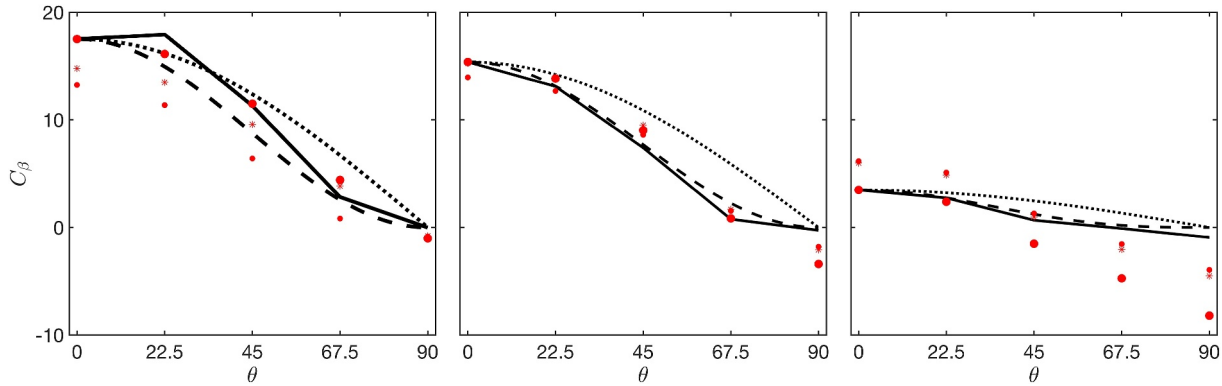

Figure 13. Wave growth/decay coefficient estimates for $c/u_* = 1.37$ (left panel), 5.48 (middle panel), and 10.95 (right panel). Wave growth/decay coefficient c_β is plotted as a function of misalignment angle θ (large red circles: $c_{\beta tot}$, small red circles: $c_{\beta p}$, and small stars: $c_{\beta p} + c_{\beta n}$). Dashed, dotted, and solid lines show $\cos(\theta)$, $\cos^2(\theta)$, and $A\ (u_{\lambda/2} \cos(\theta_w) - c)|u_{\lambda/2} \cos(\theta_w) - c|$ dependence of $c_{\beta tot}$ (see text for more information).

The existing models of sea-state dependent drag coefficient assume that the positive wave form drag contributes to increasing the drag coefficient (Chen, Ginis, & Hara, 2020; Chen, Hara, & Ginis, 2020; Donelan et al., 2012; Reichl et al., 2014). However, our LES results show that the drag reduction may occur even if the wave form drag is positive (e.g., $c/u_* = 1.37$ and $\theta = 67.5°$). Even when the wave form drag is negative (e.g., $c/u_* = 10.95$ and $\theta = 90°$), its magnitude is too small to explain the significant drag reduction. Therefore, the existing models need to be substantially modified to correctly predict the drag reduction by misaligned surface waves.

One possible way to interpret the wind-wave misaligned conditions is to redefine the wave age based on the along-wave component (component in the wave propagation direction) of the wind speed instead of the wind speed magnitude (or the wind stress magnitude). Then, as the misalignment angle increases, the wave age increases and wind-driven wave conditions transition to wave-driven wind conditions. This modified wave age is useful for understanding the wave form drag. In fact, the form drag parameterization of Donelan et al. (2012) is based on this idea. However, this modified wave age is not likely as useful for understanding the drag coefficient because the drag reduction can occur even when the modified wave age is small enough to make the wave form drag positive. Furthermore, Patton et al. (2019) show that in wave-driven wind conditions the drag coefficient increases as swell becomes more misaligned from wind (from 0° to 90°). In this case, as the modified wave age increases, the drag coefficient increases, which is opposite to our finding in this study. It suggests that the wind-driven wave regime and wave-driven wind regime are very different, whether aligned or misaligned.

It is not straightforward to quantitatively compare our LES results to the recent observational studies of drag reduction by misaligned dominant waves. This is because our LES is ran over a single wave train while the drag coefficient in the real ocean depends on a spectrum of waves, which is often quite complex. Nevertheless, the physical processes associated with the drag reduction, found in this study, may be responsible for the drag reduction in field conditions as well.

We also note that previous engineering studies report reduction of the drag coefficient over spanwise surface perturbations compared to over a flat surface (Klumpp et al., 2010). However, in these studies the turbulence modifications mainly occur inside or near the viscous sublayer (which we do not resolve), and they do not find the wind shear enhancement further above, which is the main signature of our results. Therefore, we speculate that the mechanism of drag reduction in this study is different from those reported in the engineering literature.

Finally, in this study we have investigated different wind directions and different wave ages but have used fixed values of the wave slope, the background roughness, and the surface drift velocity. We have also used a linear wave shape for the bottom boundary condition. It is desirable to conduct more comprehensive sensitivity studies varying these variables before a new parameterization of the drag coefficient over misalignment waves is developed.

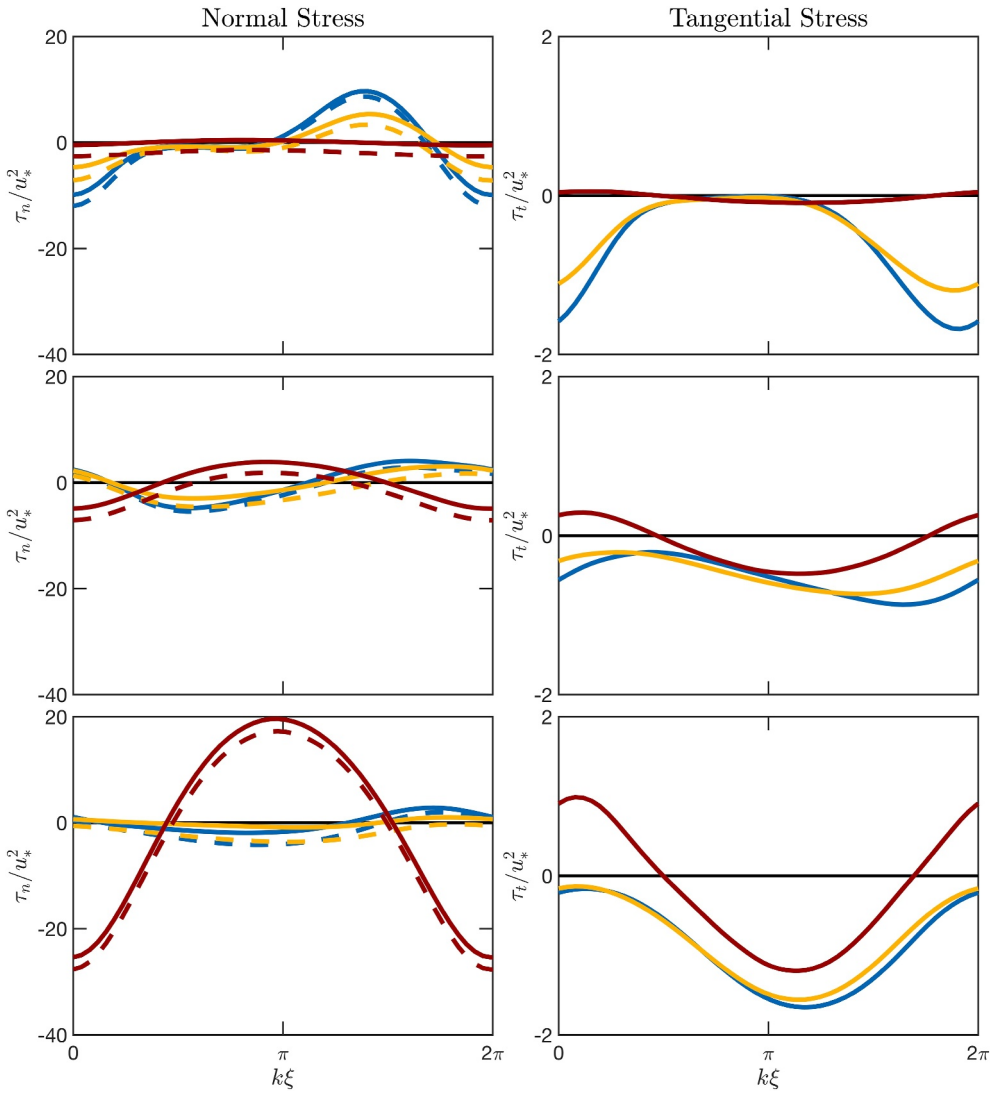

Figure 14. Surface stress distribution for normal stress $\left(\overline{\tau_n}/u_*^2\right)$ on left column (with solid lines for total normal stress and dashed lines for pressure only) and tangential stress $\left(\overline{\tau_t}/u_*^2\right)$ on right column. Results shown for $\theta = 0, 45, 90$ (blue, orange, dark red). Top rows show $c/u_* = 1.37$, middle rows $c/u_* = 5.48$, and bottom rows $c/u_* = 10.95$.

Data Availability Statement

All large eddy simulation data created and used for this study are openly available at Manzella (2023).

Acknowledgments
We acknowledge support of the National Science Foundation (Physical Oceanography) Grant OCE-2048752 (URI). We also acknowledge high-performance computing support from Cheyenne https://doi.org/10.5065/D6RX99HX provided by NCAR's Computational and Information Systems Laboratory, sponsored by the National Science Foundation. We thank Dr. Nyla Husain for her assistance throughout this study.

References

Banner, M. L. (1990). The influence of wave breaking on the surface pressure distribution in wind—wave interactions. *Journal of Fluid Mechanics*, *211*, 463–495. https://doi.org/10.1017/S0022112090001653

Belcher, S. E., Newley, T. M. J., & Hunt, J. C. R. (1993). The drag on an undulating surface induced by the flow of a turbulent boundary layer. *Journal of Fluid Mechanics*, *249*(1), 557. https://doi.org/10.1017/S0022112093001296

Cao, T., Deng, B.-Q., & Shen, L. (2020). A simulation-based mechanistic study of turbulent wind blowing over opposing water waves. *Journal of Fluid Mechanics*, *901*, A27. https://doi.org/10.1017/jfm.2020.591

Chen, X., Ginis, I., & Hara, T. (2020a). Impact of shoaling ocean surface waves on wind stress and drag coefficient in coastal waters: 2. Tropical cyclones. *Journal of Geophysical Research*, *125*(7), e2020JC016223. https://doi.org/10.1029/2020JC016223

Chen, X., Hara, T., & Ginis, I. (2020b). Impact of shoaling ocean surface waves on wind stress and drag coefficient in coastal waters: 1. Uniform wind. *Journal of Geophysical Research*, *125*(7), e2020JC016222. https://doi.org/10.1029/2020JC016222

Donelan, M. A., Babanin, A. V., Young, I. R., & Banner, M. L. (2006). Wave-follower field measurements of the wind-input spectral function. Part II: Parameterization of the wind input. *Journal of Physical Oceanography*, *36*(8), 1672–1689. https://doi.org/10.1175/JPO2933.1

Donelan, M. A., Curcic, M., Chen, S. S., & Magnusson, A. K. (2012). Modeling waves and wind stress. *Journal of Geophysical Research*, *117*(C11). https://doi.org/10.1029/2011JC007787

Donelan, M. A., Dobson, F. W., Smith, S. D., & Anderson, R. J. (1993). On the dependence of sea surface roughness on wave development. *Journal of Physical Oceanography*, *23*(9), 2143–2149. https://doi.org/10.1175/1520-0485(1993)023⟨2143:OTDOSS⟩2.0.CO;2

Donelan, M. A., Haus, B. K., Reul, N., Plant, W. J., Stiassnie, M., Graber, H. C., et al. (2004). On the limiting aerodynamic roughness of the ocean in very strong winds. *Geophysical Research Letters*, *31*(18), L18306. https://doi.org/10.1029/2004GL019460

Edson, J. B., Jampana, V., Weller, R. A., Bigorre, S. P., Plueddemann, A. J., Fairall, C. W., et al. (2013). On the exchange of momentum over the open Ocean. *Journal of Physical Oceanography*, *43*(8), 1589–1610. https://doi.org/10.1175/JPO-D-12-0173.1

Hanley, K. E., Belcher, S. E., & Sullivan, P. P. (2010). A global climatology of wind–wave interaction. *Journal of Physical Oceanography*, *40*(6), 1263–1282. https://doi.org/10.1175/2010JPO4377.1

Hara, T., & Sullivan, P. P. (2015). Wave boundary layer turbulence over surface waves in a strongly forced condition. *Journal of Physical Oceanography*, *45*(3), 868–883. https://doi.org/10.1175/JPO-D-14-0116.1

Holthuijsen, L. H., Powell, M. D., & Pietrzak, J. D. (2012). Wind and waves in extreme hurricanes. *Nature*, *117*(C9), C09003. https://doi.org/10.1029/2012JC007983

Hsu, J., Lien, R., D′Asaro, E. A., & Sanford, T. B. (2019). Scaling of Dragcoefficients Underfive tropical cyclones. *Geophysical Research Letters*, *46*(6), 3349–3358. https://doi.org/10.1029/2018GL081574

Husain, N. T., Hara, T., Buckley, M. P., Yousefi, K., Veron, F., & Sullivan, P. P. (2019). Boundary layer turbulence over surface waves in a strongly forced condition: LES and observation. *Journal of Physical Oceanography*, *49*(8), 1997–2015. https://doi.org/10.1175/JPO-D-19-0070.1

Husain, N. T., Hara, T., & Sullivan, P. P. (2022a). Wind turbulence over misaligned surface waves and air–sea momentum flux. Part II: Waves in oblique wind. *Journal of Physical Oceanography*, *52*(1), 141–159. https://doi.org/10.1175/JPO-D-21-0044.1

Husain, N. T., Hara, T., & Sullivan, P. P. (2022b). Wind turbulence over misaligned surface waves and air–sea momentum flux. Part I: Waves following and opposing wind. *Journal of Physical Oceanography*, *52*(1), 119–139. https://doi.org/10.1175/JPO-D-21-0043.1

Klumpp, S., Meinke, M., & Schröder, W. (2010). Drag reduction by Spanwise transversal surface waves. *Journal of Turbulence*, *11*, N22. https://doi.org/10.1080/14685248.2010.494606

Makin, V. K., & Kudryavtsev, V. N. (1999). Coupled sea surface-atmosphere model: 1. Wind over waves coupling. *Journal of Geophysical Research*, *104*(C4), 7613–7623. https://doi.org/10.1029/1999JC900006

Manzella, E. (2023). JGR_2023_Reduction_of_Drag_Coefficient_due_to_misaligned_surface_waves [Dataset]. *Mendeley Data, V1*. https://doi.org/10.17632/8k3w6tynwz.1

Moeng, C.-H. (1984). A large-eddy-simulation model for the study of planetary boundary-layer turbulence. *Journal of the Atmospheric Sciences*, *41*(13), 2052–2062. https://doi.org/10.1175/1520-0469(1984)041⟨2052:ALESMF⟩2.0.CO;2

Moeng, C.-H., & Sullivan, P. (2015). Large eddy simulation. In *Encyclopedia of atmospheric sciences* (2nd ed., pp. 232–240).

Patton, E. G., Sullivan, P. P., Kosović, B., Dudhia, J., Mahrt, L., Žagar, M., & Marić, T. (2019). On the influence of swell propagation angle on surface drag. *Journal of Applied Meteorology and Climatology*, *58*(5), 1039–1059. https://doi.org/10.1175/JAMC-D-18-0211.1

Potter, H., Collins III, C., & Ortiz-Suslow, D. (2022). Pier-based measurements of air-sea momentum fluxes over shoaling waves during dunex. *Journal of Geophysical Research: Oceans*, *127*(11), e2022JC018801. https://doi.org/10.1029/2022JC018801

Powell, M., Vickery, P., & Reinhold, T. (2003). Reduced drag coefficient for high wind speeds in tropical cyclones. *Nature*, *422*(6929), 279–283. https://doi.org/10.1038/nature01481

Reichl, B. G., Hara, T., & Ginis, I. (2014). Sea state dependence of the wind stress over the ocean under hurricane winds. *Journal of Geophysical Research*, *119*(1), 30–51. https://doi.org/10.1002/2013JC009289

Sheng, C., Qiao, F.-L., Zhang, J., Xue, Y., Ma, H., & Chen, S. (2022). Observed drag coefficient asymmetry in a tropical cyclone. *Journal of Geophysical Research*, *127*(9), e2021JC018360. https://doi.org/10.1029/2021JC018360

Sullivan, P. P., McWilliams, J. C., & Patton, E. G. (2014). Large-eddy simulation of marine atmospheric boundary layers above a spectrum of moving waves. *Journal of the Atmospheric Sciences*, *71*(11), 4001–4027. https://doi.org/10.1175/JAS-D-14-0095.1

Zhou, X., Hara, T., Ginis, I., D'Asaro, E., Hsu, J.-Y., & Reichl, B. G. (2022). Drag coefficient and its sea state dependence under tropical cyclones. *Journal of Physical Oceanography*, *52*(7), 1447–1470. https://doi.org/10.1175/JPO-D-21-0246.1